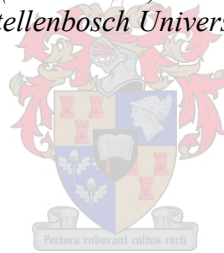


Analysing the Performance of a Compressor Impeller for a Micro Gas Turbine

by
Marco Bindeman

*Thesis presented in partial fulfilment of the requirements for the degree
of Master of Engineering (Mechanical) in the Faculty of Engineering at
Stellenbosch University*



Supervisor: Prof. S.J. van der Spuy
Co-supervisor: Prof. T.W. von Backström

April 2019

Declaration

By submitting this thesis electronically, I declare that the entirety of the work contained therein is my own, original work, that I am the sole author thereof (save to the extent explicitly otherwise stated), that reproduction and publication thereof by Stellenbosch University will not infringe any third party rights and that I have not previously in its entirety or in part submitted it for obtaining any qualification.

Date:April 2019.....

Copyright © 2019 Stellenbosch University
All rights reserved.

Plagiarism Declaration

1. Plagiarism is the use of ideas, material and other intellectual property of another's work and to present it as my own.
2. I agree that plagiarism is a punishable offence because it constitutes theft.
3. I also understand that direct translations are plagiarism.
4. Accordingly all quotations and contributions from any source whatsoever (including the internet) have been cited fully. I understand that the reproduction of text without quotation marks (even when the source is cited) is plagiarism.
5. I declare that the work contained in this assignment, except where otherwise stated, is my original work and that I have not previously (in its entirety or in part) submitted it for grading in this module/assignment or another module/assignment.

Student number	Signature
<i>M. Bindeman</i>	21/02/2019
Initials and surname	Date

Abstract

Analysing the Performance of a Compressor Impeller for a Micro Gas Turbine

M. Bindeman

*Department of Mechanical and Mechatronic Engineering,
University of Stellenbosch,
Private Bag X1, Matieland 7602, South Africa.*

Thesis: MEng (Mech)

April 2019

This project sets out to numerically evaluate the performance of micro gas turbine (MGT) compressor impellers and to improve the 1-Dimensional (1-D) mean-line code developed for the in-house analysis of these impellers. The objective for the improvement of the code is to accurately predict the performance of both radial flow and mixed-flow impellers. The possible applications for MGTs are numerous. They find specific application for the propulsion of unmanned aerial vehicles (UAVs). Mixed-flow compressors offer the opportunity to reduce the frontal area of a MGT engine while maintaining a high pressure ratio and ensuring a high thrust-to-weight ratio. The use of mixed-flow impellers in MGTs are thus attractive. Although detailed aerodynamic design is normally based on two- and three-dimensional viscous flow analysis, 1-D analysis with empirical work input and loss models is the basis for most aerodynamic performance analyses. Using 1-D mean-line flow analyses also allows the researcher to analyse multiple geometries in a short time span, while only analysing the best performing geometries with 3-D Computational Fluid Dynamics (CFD). Two areas of the mean-line code were identified for improvement. A new slip factor formulation taking both radial and axial flow components into account was implemented. Secondly, an alternative location for the inter-blade throat area was proposed, considering the area between a main blade and splitter blade, as opposed to the area close to the inducer section which is effectively between the main blades. The code was adapted to calculate the throat parameters for the alternative location and two iterations

ABSTRACT

v

of the code were subsequently created. The first employing the new slip factor and the second employing both the new slip factor and an alternative throat location. Three different impellers, of which one impeller is a mixed-flow impeller, were analysed using the adapted mean-line code and the results were validated with 3-dimensional CFD. The newly adapted 1-D mean-line code was found to predict the performance of the mixed-flow impeller reasonably well. The mean-line code over predicted both the pressure ratio and isentropic efficiency (total-to-total) by 1.6% and 2.8% respectively, while also predicting a larger operating range. The pressure ratio of the centrifugal impellers was under predicted on average by 15%, while the the isentropic efficiency was predicted within 3%. It was however found that a blade outlet angle of 90° adversely affected the performance prediction of the code.

Keywords: micro gas turbine, mixed-flow compressor, one dimensional mean-line code.

Uittreksel

Analise van die Werksverrigting van n Kompressor Rotor vir n Mikro-gasturbine

(“Analysing the Performance of a Compressor Impeller for a Micro Gas Turbine”)

M. Bindeman

*Departement Meganiese en Megatroniese Ingenieurswese,
Universiteit van Stellenbosch,
Privaatsak X1, Matieland 7602, Suid Afrika.*

Tesis: MIng (Meg)

April 2019

Hierdie projek beoog om numeries die prestasie van mikro-gasturbine kompressors rotor te evalueer, asook die 1-dimensionele (1-D) werkverrigting-berekeningskode wat ontwikkel is vir 'n interne analise van die rotors. Die mikpunt van die verbeterde kode is om die prestasie van die radiale vloeï en die gemengde-vloeï rotors akkuraat te voorspel. Daar is vele moontlike toepassings vir mikro-gasturbines. Mikro-gasturbines kan spesifiek gebruik word vir die aandrywing van onbemande vliegtuie. Gemengde-vloeï kompressors bied die geleentheid om die voorste area van 'n mikro-gasturbine-enjin te verklein, terwyl dit 'n hoë drukverhouding en 'n dryfkrag-tot-gewig verhouding behou. Die gebruik van gemengde-vloeï rotors in mikro-gasturbines is dus aanloklik. Al is gedetailleerde aërodinamiese ontwerpe gewoonlik gebaseer op 2- of 3-dimensionele viskeuse vloeï-analise, is 1-dimensionele analyses met empiriese werksinsette en werksuitsette se modelle die basis vir die meeste aërodinamiese prestasie-analises. Deur die 1-D werkverrigting-berekeningvloeï analise te gebruik, kan die navorser ook meervoudige geometrieë analiseer in 'n kort tydperk, deur slegs die hoogs presterende geometrieë te analiseer met 3-D berekenings vloeïdinamika. Twee areas van die werkverrigting-berekeningskode is geïdentifiseer om te verbeter. 'n Nuwe glijfaktor formulering, wat beide die radiale en die aksiale vloeï komponente in ag neem, is geïmplementeer. Tweedens is 'n alternatiewe posisie vir die inter-lem keëlarea voorgestel, wat die area tussen die hooflem en die sekondêre lem in ag neem, eerder as die area

naby die inlaat wat effektief tussen die hooflemme is. Die kode is aangepas om die keëlparameters te bereken vir die alternatiewe posisie en twee iterasies van die kode is vervolgens geskep. Die eerste een is die toepassing van die nuwe glipfaktor en tweede, die toepassing van beide die nuwe glipfaktor en 'n alternatiewe keëlposisie. Drie verskillende rotors, waarvan een 'n gemengde-vloei rotor was, is geanaliseer deur die aangepaste werkverrigting-berekeningskode te gebruik en die resultate is gevalideer met 3-dimensionele berekenings vloeddinamika. Die nuut aangepaste 1-D werkverrigting-berekeningskode het bevind dat die voorspelling van die gemengde-vloei rotors se prestasie, redelik goed is. Die werkverrigting-berekeningskode het beide die drukverhouding en die isentropiese doeltreffendheid (totaal-tot-totale) met 1,6% en 2,8% afsonderlik oorskat, terwyl dit ook 'n groter werksbestek voorspel het. Die drukverhouding van die sentrifugale rotors was onderskat met 'n gemiddelde 15%, terwyl die isentropiese doeltreffendheid voorspel was binne 3%. Dit is wel bevind, dat die lem se uitlaathoek van 90° 'n nadelige effek op die prestasievoorspelling van die kode het.

Sleutelwoorde: mikro gasturbine, gemengde-vloei kompressors, een-dimensionele werkverrigting-berekeningskode.

Acknowledgements

My acknowledgements go to the following individuals and institutions to whom I wish to express my sincere appreciation and gratitude for accompanying me on my MEng journey:

- First and foremost I want to thank God for His faithfulness and immeasurable grace. He strengthened me and provided me with hope beyond that which the world can offer. I thank Him for saving me and giving me life, and providing me with the opportunity to complete this thesis. "For from Him and through Him and to Him are all things. To Him be glory forever. Amen."
- My dad, Franco Bindeman and my grandparents, Rob and Mavis Guthrie. They supported me financially, emotionally and most important in prayer. Thank you for always believing in me and calling out the best in me. I learned from you to never give up, but instead to see a challenge as a chance to grow in character.
- My two supervisors, Prof. S. J. van der Spuy and Prof. T. W. von Backström, for their guidance, patience, and invaluable wisdom regarding turbomachinery. Also to Prof. van der Spuy, for his support in finding and providing funding for this project. I learned from you to work hard and to do so with excellence. I also learned to keep on searching and to dig deeper until a reason or solution can be provided.
- To Holger Dietrich for his never ending and timely help with Numeca.
- To my girlfriend, Karla Brand, for her support and help throughout the two years. I learned from you that it is okay to sometimes take a time out and to return to a problem with a fresh perspective.
- CSIR, CONVERGE as well as ARMSCOR for the funding of this project.
- To the staff in charge of the high performance cluster at Stellenbosch University.

Dedications

To my Mom...

Contents

Declaration	ii
Abstract	iv
Uittreksel	vi
Acknowledgements	viii
Dedications	ix
Contents	x
List of Figures	xiii
List of Tables	xv
Nomenclature	xvi
1 Introduction	1
1.1 Background	1
1.2 Motivation	2
1.3 Objectives	3
1.4 Thesis Outline	4
1.5 Previous Research	4
2 Literature Study	7
2.1 Micro Gas Turbine	7
2.2 Mixed-Flow Compressors	8
2.3 Basic Compressor Theory	11
2.4 Impeller Performance	13
2.5 Slip	15
2.6 Splitter Blades	17

2.7	Compressor Instabilities	18
3	Mean-Line Code	20
3.1	Introduction	20
3.2	Code Structure	21
3.3	Code Inputs	21
3.4	Impeller Geometry	22
3.4.1	Endwalls	23
3.4.2	Blades	24
3.5	Impeller Performance	27
3.6	Code Output	28
3.7	Adjustment of the In-House Code	28
3.7.1	Slip Formulation	28
3.7.2	Throat Area	36
3.8	Summary	40
4	Computational Fluid Dynamics	41
4.1	Introduction	41
4.2	Impeller Geometry	41
4.2.1	Geometry File Format	42
4.2.2	Geometric Scans	43
4.3	Computational Domain	44
4.4	Mesh Generation	45
4.5	Fluid and Flow Model	50
4.6	Boundary Conditions	51
4.7	Settings	53
4.8	Post-processing	56
4.9	Summary	56
5	Results and Discussion	57
5.1	Mean-Line Code Results	57
5.2	k27 Impeller	59
5.3	Van der Merwe Impeller	62
5.4	Diener Impeller	66
5.5	Summary	68
6	Conclusions and Recommendations	69
6.1	Conclusions	69
6.2	Recommendations	71
	List of References	72

<i>CONTENTS</i>	xii
Appendix A: Impeller Geometry Parameters	76
Appendix B: Mean-Line Code Flow Charts	79
Appendix C: <i>geomTurbo</i> File Format	83
Appendix D: Compressor Maps	85
Appendix E: CFD Grid Dependency	90

List of Figures

1.1	KKK k27 Centrifugal Compressor Impeller (Van der Merwe, 2012) . . .	5
1.2	Van der Merwe Optimised Centrifugal Impeller (Van der Merwe, 2012)	6
1.3	Diener Impeller	6
2.1	Components of a typical MGT. Adapted from Wehrly (2014)	8
2.2	Mixed-Flow Compressor Components in the Meridional Plane (Diener, 2016)	10
2.3	Mixed-Flow Compressor Impeller Velocity Triangles (Diener, 2016) . . .	11
2.4	Mollier Chart for a Compressor	12
2.5	Overall Characteristic of a Compressor (Dixon, 1998)	15
2.6	Velocity Triangle at the Outlet of a Backswept Impeller (Ji <i>et al.</i> , 2010)	15
2.7	Coriolis Circulation in a Centrifugal Impeller	17
2.8	Rotating Stall in a Centrifugal Compressor Inducer (Boyce, 1993) . . .	18
3.1	Meridional View of Endwall Contours and Bézier Control Points	24
3.2	Definition of the Blade Camber Line by β angle (Verstraete <i>et al.</i> , 2010)	25
3.3	Blade Thickness Distribution Normal to the Camber Line (not to scale) (Verstraete <i>et al.</i> , 2010)	26
3.4	Various Slip Factors for Eckardt's Rotor 'A'	30
3.5	Different Slip Factors (Pfleiderer's definition) for the Eckardt Rotor A .	35
3.6	Different Slip Factors for the k27 Rotor	35
3.7	Quasi-Normal Geometry	36
3.8	Throat in Transformed Plane	38
4.1	Curves and Surfaces Defining k27 Impeller Geometry	42
4.2	k27 Computational Domain	44
4.3	Diener Impeller Computational Domain	45
4.4	y^+ Values of the k27 Impeller at Design Point. $m_{design}=0.277$ kg/s . . .	47
4.5	k27 Impeller H&I Topology for Main and Splitter Blades	48
4.6	Final Mesh for the k27 Impeller	50
4.7	Periodic Boundary Connections	52

LIST OF FIGURES

xiv

4.8	Global Convergence History	55
4.9	Mass Flow Convergence History	55
5.1	Results Comparison for the k27 Rotor at 121 krpm	60
5.2	Different Computational Domains for the k27 Impeller	61
5.3	Relative Mach Number at 90% Span for the k27 Impeller	62
5.4	1-D Mean-line comparison of Van der Merwe mean-line rotor at 121 krpm. $m_{design} = 0.325$ kg/s	63
5.5	1-D Mean-line comparison of Van der Merwe optimised rotor at 121 krpm. $m_{design} = 0.325$ kg/s	64
5.6	Results Comparison for the Optimised Van der Merwe Impeller at 121 krpm. $m_{design} = 0.325$ kg/s	66
5.7	Results Comparison for the Final Diener Impeller at 95 krpm. $m_{design} =$ 0.85 kg/s	67
5.8	Relative Mach Number at 90% Span for the Optimised Diener Impeller	68
B.1	Flow Diagram of the in-house Design Code (Van der Merwe, 2012) . .	80
B.2	Flow Diagram for the getPerformance Matlab Script	81
B.3	Flow Diagram for the displayChart Matlab Script	82
D.1	k27 Impeller Compressor Map	86
D.2	Van der Merwe mean-line Impeller Compressor Map	87
D.3	Van der Merwe Optimised Impeller Compressor Map	88
D.4	Diener Optimised Impeller Compressor Map	89

List of Tables

1.1	CFD Results for Impeller Comparison (Van der Merwe, 2012)	5
3.1	Free Parameters of Van der Merwe (2012) Rotor	22
3.2	K27 Main Parameters	23
3.3	Thickness Distribution Parameters for the k27 Impeller	26
3.4	Target Values for Respective Impellers	28
3.5	Main Geometrical Parameters for the Eckardt Rotor 'A'	30
3.6	Ji <i>et al.</i> Slip Factor Results. Adapted from Ji <i>et al.</i> (2010)	32
3.7	SRE Slip Factors Compared to Predictions by other Authors, for RR=0.5 and $\beta = 50^\circ$	33
4.1	k27 Mesh Quality	49
4.2	Van der Merwe optimised impeller Mesh Quality	49
4.3	Diener impeller Mesh Quality	49
4.4	Inlet Boundary Imposed Quantities	52
5.1	Summary of Performance Results for the Different Code Iterations for Different Rotors	58
A.1	Main Geometrical Parameters for the k27 Impeller	76
A.2	Main Geometrical Parameters for the Van der Merwe m-l Impeller	77
A.3	Main Geometrical Parameters for the Van der Merwe optimised Impeller	77
A.4	Main Geometrical Parameters for the Diener optimised Impeller	78
E.1	Mesh Dependency Study for the k27 Impeller	90
E.2	Mesh Dependency Study for the Van der Merwe Impeller	91
E.3	Mesh Dependency Study for the Diener Impeller	91

Nomenclature

Abbreviations

ANN	Artificial neural network
CAD	Computer aided design
CFD	Computational fluid dynamics
CFL	Courant-Friedrich-Levy
CL	Clearance Gap
GUI	Graphical User Interface
<i>IGES</i>	Three-dimensional computer model format
KKK	Kuhnle, Kopp & Kausch
LE	Leading edge
MEP	Maximum efficiency point
MGT	Micro gas turbine
m-l	Mean-Line
NACA	National Advisory Committee for Aeronautics
RR	Radius Ratio
SRE	Single Relative Eddy
<i>stl</i>	Stereolithography
TE	Trailing edge
UAV	Unmanned aerial vehicle
1-D	One-dimensional
3-D	Three-dimensional

Symbols

A	Area	$[m^2]$
A_R	Passage area ratio	$[-]$
A_t	Blade passage throat area ratio	$[-]$

NOMENCLATURE

xvii

b	Blade height	[m]
C	Absolute fluid velocity	[m/s]
c	Blade length	[m]
D_{eq}	Equivalent diffusion factor	[-]
d	Diameter	[m]
dm	Meridional length along meridional co-ordinate m	[-]
F	Shape factor, solidity influence coefficient	[-, -]
$f_{startsplit}$	Splitter fraction of main blade length	[-]
h	Specific enthalpy, hub control point	[J/kg, -]
h_t	Throat width	[m]
I	Rothalpy, Work input coefficient	[J/kg, -]
K	Diffuser camber line constant	[-]
L	Length	[m]
m	Mass, meridional length, meridional co-ordinate	[kg, m, -]
N	Rotational speed	[rpm]
n	station or state, distance along a quasi-normal	[-, -, m]
P	Penalty term value	[-]
p	pressure, parameter	[Pa, -]
r	Radius, radial co-ordinate	[m, -]
s	Entropy, shroud control point, blade pitch	[kJ/kg K, -, m]
T	Temperature	[K]
t	Blade thickness, clearance gap	[m]
U	Blade velocity	[m/s]
u	Non-dimensionalised length	[-]
V	Velocity	[m/s]
W	Relative fluid velocity, specific work done	[m/s, J/kg]
$x - y - z$	Cartesian co-ordinates	[-]
y	Distance	[m]
Z, z	Number of blades, axial co-ordinate	[-, -]
∂	Partial derivative	[-]
\in	Is a member of	[-]

Greek symbols

α_C	Streamline slope angle with the axial co-ordinate . . .	[°]
β	Blade camber angle	[rad]
γ	Specific heat ratio	[–]
Δ	Difference	[–]
ϵ	Deviation of a quasi-normal from a true normal	[°]
η	Isentropic efficiency	[–]
θ	End wall contour angle, blade camber circumferential position, tangential co-ordinate	[rad, rad, °]
λ	Impeller tip distortion factor	[–]
μ	Mutation rate	[–]
ν	Kinematic viscosity	[m ² /s]
Π	Pressure ratio	[–]
ρ	Density	[kg/m ³]
σ	Slip factor	[–]
ϕ_2	Tip flow coefficient	[–]
Ω	Rotor angular velocity	[–]
ω	Rotational speed, vorticity	[rad/s, –]
$\bar{\omega}_{cr}$	Supercritical Mach number loss coefficient	[–]
$\bar{\omega}_{mix}$	Mixing loss coefficient	[–]

Subscripts

0	Compressor inlet
0n	Total condition, stagnation condition
1	Impeller inlet
2	Impeller tip
3	Diffuser outlet
B, b	Bézier control point, blade parameter
CL	Camber line quantity
<i>design</i>	Specified design condition
e	Exit of impeller
H, h	Hub quantity
<i>hub</i>	Hub quantity
<i>imp</i>	Impeller

NOMENCLATURE

xix

<i>lim</i>	Limiting
<i>m</i>	Meridional component
<i>main</i>	Main blade quantity
<i>max</i>	Maximum quantity
<i>n</i>	Compressor section
<i>QN</i>	Parameter on a quasi-normal
<i>r, θ, z</i>	Cylindrical co-ordinate components
<i>ref</i>	Reference quantity
<i>S, s</i>	Shroud, isentropic process, stall condition, slip
<i>shroud</i>	Shroud quantity
<i>slip</i>	Slip condition
<i>split</i>	splitter blade quantity
<i>t – t</i>	Total-to-total quantity
<i>t</i>	Total condition
<i>th</i>	Quantity at throat
<i>U</i>	Tangential velocity component
<i>wall</i>	Condition at the wall
<i>x, y, z</i>	Cartesian co-ordinate components

Superscripts

\cdot	Time rate of change
$+$	Dimensionless wall distance indicator
$'$	Infinite number of blades

Chapter 1

Introduction

This thesis aims to adapt an already existing 1-D mean-line code for compressors to include mixed-flow impellers and compare the results to CFD analysis. The two impellers under consideration were developed by Van der Merwe (2012) (centrifugal) and Diener (2016) (mixed-flow).

1.1 Background

The possible applications for MGTs are numerous and include portable power generation, residential and small commercial backup power or cogeneration and marine power generation (Krige, 2013; Shukla, 2013; Vick *et al.*, 2010). Aircraft propulsion, such as in unmanned aerial vehicles (UAVs), completes the list of possible applications and is the focus for the impeller designed by Diener (2016).

This study specifically considers the compressor stage of an MGT with the focus on the impeller section of the stage. Both axial and centrifugal compressors are used in the aerospace industry. Centrifugal compressors are preferred above axial compressors for MGTs, because only one stage is usually required, compared to multiple compressor stages in an axial compressor, to achieve a specific pressure ratio. Centrifugal compressors do however have a drawback in that they require a larger diameter to produce the required pressure ratio in one stage. For aerospace application, this is important, as the drag of a MGT is proportional to its frontal area. Mixed-flow compressor impellers potentially allow the radius of the rotor to be reduced, leading to a reduction in frontal area and lower drag for the engine. Mixed-flow compressors also have a relatively high mass flow rate compared to centrifugal compressors and together with the possibility of achieving a high pressure ratio in one stage sets the mixed-flow compressor apart to be implemented in a certain range of MGTs used for UAVs.

Pressure ratio and efficiency versus mass flow rate are the main parameters used when analysing the performance of a compressor impeller (Diener, 2016). The most common way to analyse these parameters is to do a three-dimensional (3-D) Computational Fluid Dynamics (CFD) analysis; however, this can be computationally expensive and time consuming. A one-dimensional (1-D) analysis is inexpensive and allows the user to analyse multiple geometries in a short time span.

This document addresses the amendment of the in-house, one-dimensional code, written in Matlab[®] by De Wet (2011) and updated by successive master's students, in order to successfully predict the performance of both centrifugal and mixed-flow impellers. A 3-D analysis is performed on various rotors to evaluate the results of the 1-D analyses.

1.2 Motivation

Since the 1990s advanced UAVs were developed, and the successful integration of MGTs into these aircraft required high performance and lower cross-sectional area engines (Cevik, 2009). These requirements eventually facilitated the introduction of mixed-flow compressors as a strategic alternative for use in a specific size of MGT. The increased interest from military and civil sectors in the application of MGTs makes the development of such an engine and its components a viable project (Marcellan, 2015). To analyse the feasibility of using these types of compressors for aero engines, several capabilities must be put in place in order to ensure that the design is effective as well as reliable. Although detailed aerodynamic design is normally based on two- and three-dimensional inviscid or viscous flow analysis, one-dimensional analysis with empirical work input and loss models is the basis for most aerodynamic performance analysis (Aungier, 2000). It is therefore important to have a 1-D code that is able to predict the performance of both centrifugal and mixed-flow impellers.

Diener (2016) has proved that a mixed-flow compressor for application in an MGT is viable, but stated that further research and development is necessary concerning the meridional exit angle. Rajakumar *et al.* (2015) states that it is well known that the interaction between a mixed-flow impeller and diffuser substantially influences the flow fields and performance of the entire compressor. Rajakumar *et al.* (2015) comments that it is, therefore, necessary to study and understand the complex flow field inside the flow channel of mixed-flow compressors. A cross-over diffuser for a mixed-flow impeller has been developed by Kock (2017) and testing of the

mixed-flow compressor has since been completed by Swanepoel (2018), although, at the time of writing, the results are not yet published.

The in-house 1-D mean-line code as developed by De Wet (2011) was modified by Diener (2016) to accommodate the meridional outlet angle, α_{e2} . This was done in order to analyse a mixed-flow impeller instead of only a radial flow impeller. Diener recorded a 22% difference between the mean-line and CFD pressure ratio and was forced to use a commercial one-dimensional layout tool, namely CFTurbo[®]. The in-house mean-line code therefore still requires further adaptation to work for both centrifugal and mixed-flow compressor configurations.

1.3 Objectives

The objective of this thesis is to evaluate the performance of both centrifugal and mixed-flow compressor impellers for MGT application. The KKK k27 impeller will be used as a benchmark rotor. Both the mean-line and optimised Van der Merwe (2012) impellers will also be analysed as well as the Diener impeller. A brief point-wise discussion of the methodology used to achieve the thesis objective are listed below:

- Complete a literature study on the design of mixed-flow compressors.
- Review the existing 1-D mean-line code and determine specific areas to be improved in order to analyse a mixed-flow impeller.
- Adapt the areas identified for improvement in the in-house 1-D mean-line code.
- Model the k27 impeller in a Computer Aided Design (CAD) package. Autodesk[®] Inventor[®] Professional 2018 is the CAD package used.
- Analyse the k27, mean-line and optimised Van der Merwe and Diener impellers in the 1-D mean-line code. The in-house code, developed by De Wet (2011) and based on centrifugal compressor theory by Aungier (2000) is used for the mean-line analysis.
- Export each impeller geometry into a 3-D Computational Fluid Dynamic software package to model and analyse the impellers. The Numeca suite of CFD software packages was used for the CFD analyses.
- Evaluate and compare the numerical results from the 1-D mean-line code to that of the 3-D CFD results.

- Draw conclusions from the evaluation of the different compressor impellers analysed and provide recommendations for future work.

1.4 Thesis Outline

The project objectives and motivation have been discussed in this chapter, along with background information on MGTs. Chapter 2 details the information gathered during the literature study and also covers the first objective.

Chapter 3 discusses the details regarding the set-up of the in-house mean-line code and the adjustments made to the code in order to reach the 2nd objective. Chapter 4 contains all the information on the setup of the 3-D computational fluid dynamics analysis.

All the results, of both the in-house mean-line code impeller performance and the adjustments made to the code, and the computational fluid dynamics analyses are discussed in Chapter 5. Finally, the project conclusion is presented in Chapter 6 along with recommendations to be considered in future studies.

1.5 Previous Research

Several projects regarding the development and optimisation of compressor impellers for micro gas turbine application have been conducted at Stellenbosch University. De Wet (2011) developed an in-house 1-D code to analyse compressor impellers. Van der Merwe (2012) focussed on the development of a new radial flow impeller for application in a 200 N thrust MGT. Krige (2013) then conducted a study on the development of a new radial diffuser for the BMT 120 KS MGT. De Villiers (2014) focussed on the simultaneous optimisation of the compressor impeller and diffuser. A diffuser section was added to the in-house mean-line code by De Villiers (2014) as part of his project. Burger (2016) went one step further by developing a single vaned crossover diffuser for the 200 N thrust engine. The focus then shifted to mixed-flow impellers for MGT application and Diener (2016) conducted the first study on mixed-flow impellers with the objective to develop a mixed-flow impeller for a 600 N MGT application. Kock (2017) designed a crossover diffuser for the Diener impeller.

The 1-D code developed by De Wet (2011) was used for many of the above-mentioned projects to create a mean-line geometry for further CFD analysis. Van der Merwe (2012) used the KKK k27 impeller to complete a benchmark analysis.

He then designed both a mean-line and optimised radial flow rotor. The mean-line rotor was designed through the use of the in-house code, and the optimised rotor was developed by optimising the mean-line rotor in the Numeca FINE™/Design environment. Figure 1.1 shows the k27 impeller, while the final optimised impeller by Van der Merwe is shown in Figure 1.2. Table 1.1 documents a comparison of the performance predicted for the two impellers. Diener (2016) made use of CFTurbo[®], after unsuccessful attempts at adapting De Wet's (2011) code for mixed-flow impellers. The impeller developed by Diener (2016) is shown in Figure 1.3.

Table 1.1: CFD Results for Impeller Comparison (Van der Merwe, 2012)

Impeller	r_2 [mm]	\dot{m} [kg/s]	Π_{t-t}	η_{t-t}
KKK k27	40.0	0.277	4.75	87%
Optimised Van der Merwe (2012)	37.5	0.336	5.34	91.6%



Figure 1.1: KKK k27 Centrifugal Compressor Impeller (Van der Merwe, 2012)



Figure 1.2: Van der Merwe Optimised Centrifugal Impeller (Van der Merwe, 2012)

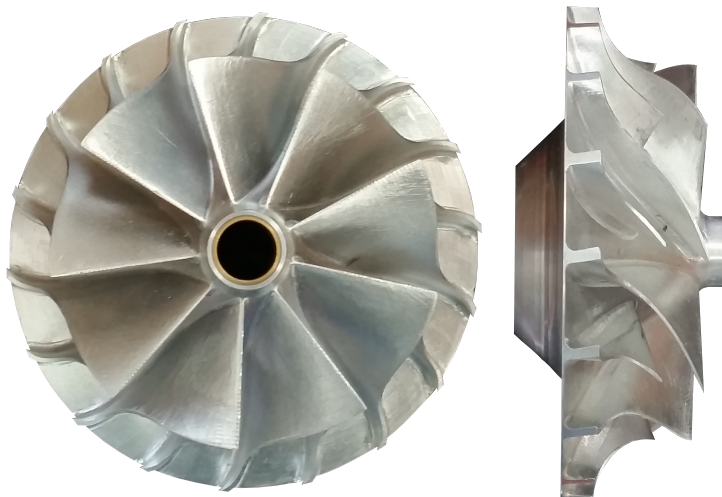


Figure 1.3: Diener Impeller

Chapter 2

Literature Study

The literature study entails a basic discussion on MGTs and a more detailed discussion on the theory concerning centrifugal compressors. The chapter includes a thorough discussion on slip within centrifugal impellers.

2.1 Micro Gas Turbine

A MGT is an engine that contains turbomachinery components. Turbomachines are devices used to transfer energy either to or from a continuously flowing fluid. This is done through the dynamic action of one or multiple moving blade rows. The stagnation enthalpy and subsequently kinetic energy, and stagnation pressure are changed by the operation of the blade rows. In the case of a compressor, the energy is imparted to the fluid, whereas in the case of a turbine the energy is extracted from the fluid (Dixon, 1998; Lakshminarayana, 1996). A MGT is essentially an engine that comprises both types of turbomachines in order to produce thrust or be used for electric power generation.

The compressor is responsible for the increase of the pressure of the air entering the machine, whereby combustion is made more effective. Before air enters the combustion chamber, fuel is added to form a fuel-air mixture that is ignited in the combustion chamber. The turbine in turn is responsible for extracting the energy of the combustion gasses and drive the compressor. The combustion gasses exiting the turbine is directed through a nozzle, forming a jet, and producing thrust. The thrust (a net reactive force) acting on the given geometry is the fundamental propulsive mechanism of a jet engine (Hill and Peterson, 1992). Figure 2.1 shows the layout of a typical MGT.

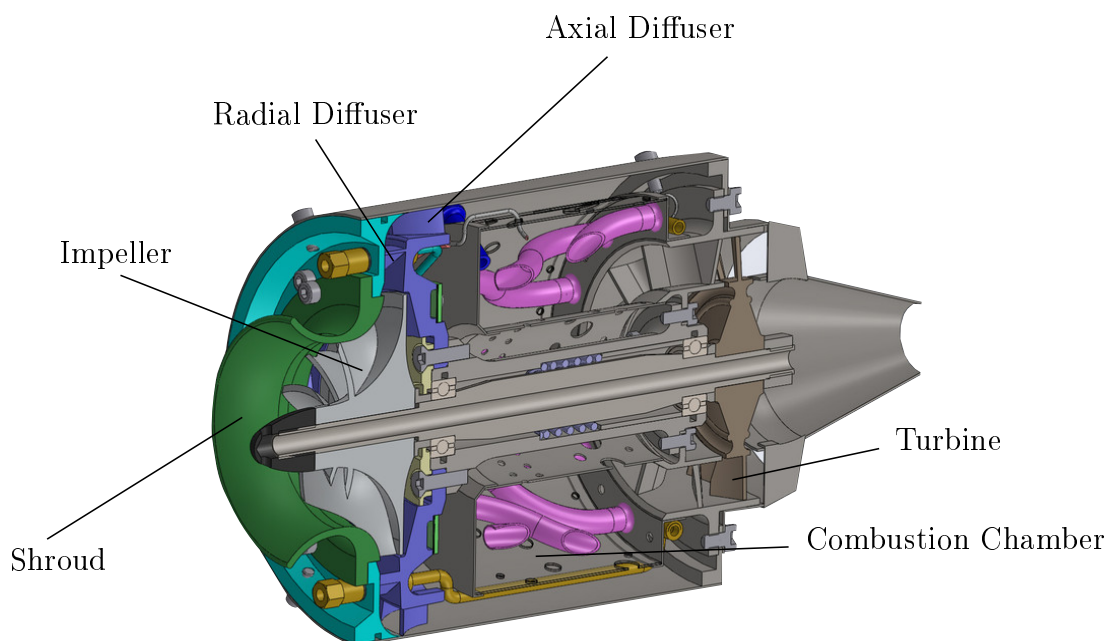


Figure 2.1: Components of a typical MGT. Adapted from Wehrly (2014)

Most aircraft engines utilise axial flow compressor rotors, centrifugal flow compressor rotors or a combination of both (Youssef and Weir, 2002). Centrifugal and mixed-flow compressors are the two conventional types of compressors used in MGTs. These two types of compressors are preferred above axial compressors due to their higher efficiency at small volume flow rates. A mixed-flow compressor is geometrically very similar to a centrifugal compressor, but with significant differences in performance (Kock, 2017). Mixed-flow compressors have a significantly higher mass flow rate and are also able to operate over a broader range of mass flow rates at specific rotational speed compared to centrifugal compressors (Saravanamuttoo *et al.*, 2001).

2.2 Mixed-Flow Compressors

Investigations into mixed-flow impellers started in the early 1940s at the National Advisory Committee for Aeronautics (NACA). King and Glodeck (1942) investigated the performance of a mixed-flow impeller and vaned diffuser unit with several modifications in a NACA variable-component supercharger test rig. High impeller efficiency (0.92) was achieved, but so was a large loss in the diffuser.

The same problems that faced centrifugal impellers hampered the work on mixed-flow impellers in the 1950s and 1960s. These were structural limitations, no experi-

mental data-base, limited computational ability, and severe problems with diffuser design (Musgrave and Plehn, 1987). In the early 1980s, Whitfield and Roberts (1981) presented a paper on the overall performance of a turbocharger compressor employing three mixed-flow impellers, reviving the interest in mixed-flow impellers. They found that flow stability was improved by the application of a mixed-flow impeller with a horizontal cut off at the vane tips. Hoping that the results of their study would stimulate further investigation into mixed-flow impellers, Musgrave and Plehn (1987) designed and tested a mixed-flow compressor stage with a pressure ratio of 3:1.

Noting that high power-to-weight ratio is a predominant requirement for small jet-engines and that the demands on the compressor can either be fulfilled by a conventional two-stage unit or by an extremely loaded single stage, Monig *et al.* (1987) discussed the possible application of a mixed-flow compressor to meet the compressor demands. Mönig *et al.* (1993) then went on to design and test a supersonic mixed-flow compressor with a pressure ratio of 5:1. Eisenlohr and Benfer (1994) designed and experimentally tested a single stage mixed-flow impeller. The impeller pressure ratio at design speed and design corrected mass flow rate met the design value of 7.5, while isentropic impeller efficiencies above 91% were recorded.

Focussing on subsonic flow Youssef and Weir (2002) developed and patented a mixed-flow/centrifugal compressor combination for a turbojet engine. Hamilton and Sundstrand have successfully developed MGTs that employ mixed-flow compressors for thrusts between 200 and 450 N (Harris *et al.*, 2003). Cevik (2009) generated a mixed-flow impeller using the individual design methodology he developed for a centrifugal impeller. The impeller has a pressure ratio of 4.34 at a rotational speed of 120000 rpm. Diener (2016) developed a mixed-flow impeller with a simulated pressure ratio of 5.25 and isentropic efficiency of 86%. Diener made use of coupled aero-mechanical optimisation, using FINE™/Design3D v. 9-1.3, to obtain his final impeller design.

Figure 2.2 shows the different entities of a mixed-flow impeller. The meridional plane is used to define the hub, shroud, main and splitter blade leading edge (LE) and trailing edge (TE) shapes of a turbomachine.

The meridional exit angle is shown by α_{e2} . For a centrifugal compressor, this exit angle will be 90° . The air enters the compressor impeller through the inducer, also known as the impeller eye. The air may enter the inducer with a pure axial velocity or with whirl, which is an added tangential component to the flow. In high pressure ratio compressors, it may be necessary to impart whirl to the inlet flow as a means of reducing high relative inlet velocity (Dixon, 1998). The leading

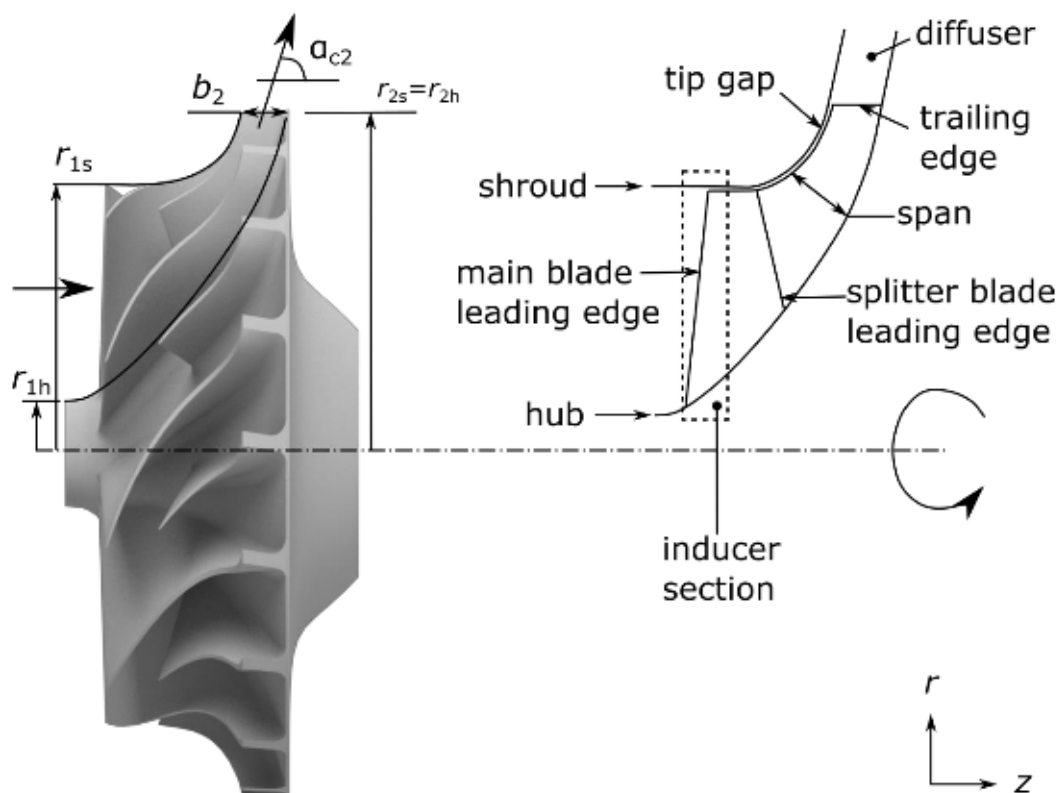


Figure 2.2: Mixed-Flow Compressor Components in the Meridional Plane (Diener, 2016)

edge of the main blade scoops the air at an absolute velocity C_1 , a relative fluid velocity W_1 and a blade tip velocity U_1 and directs it towards the blade passage. Once the air is aligned with the blades, it is accelerated by the blades and moves along the blade passage. The work imparted by the impeller causes an increase in the pressure and temperature of the air from the inlet to the outlet of the impeller.

At the outlet of the impeller, the air leaves the TE of the blades and proceeds to the diffuser. In case of a mixed-flow compressor, the air exits the impeller with a radial velocity C_{r2} , axial velocity C_{z2} , and tangential velocity $C_{\theta 2}$. The absolute impeller exit velocity is given by C_2 . The flow does however not leave the blades at exactly β_2 due to a phenomenon called slip. Slip decreases the ideal tangential velocity $C_{\theta 2}$ by $\Delta C_{\theta 2}$. The flow decreases in speed in the diffuser at a loss of total pressure, but with a gain in static pressure. The type and shape of the diffuser determines the magnitude of this loss. Figure 2.3 shows the velocity triangles of a mixed-flow impeller. Here the axial component of flow due to the mixed-flow

impeller, as opposed to a centrifugal impeller can be visualised from the impeller exit velocity triangles. Decreasing the meridional exit angle ($< 90^\circ$) will cause the axial velocity component to increase.

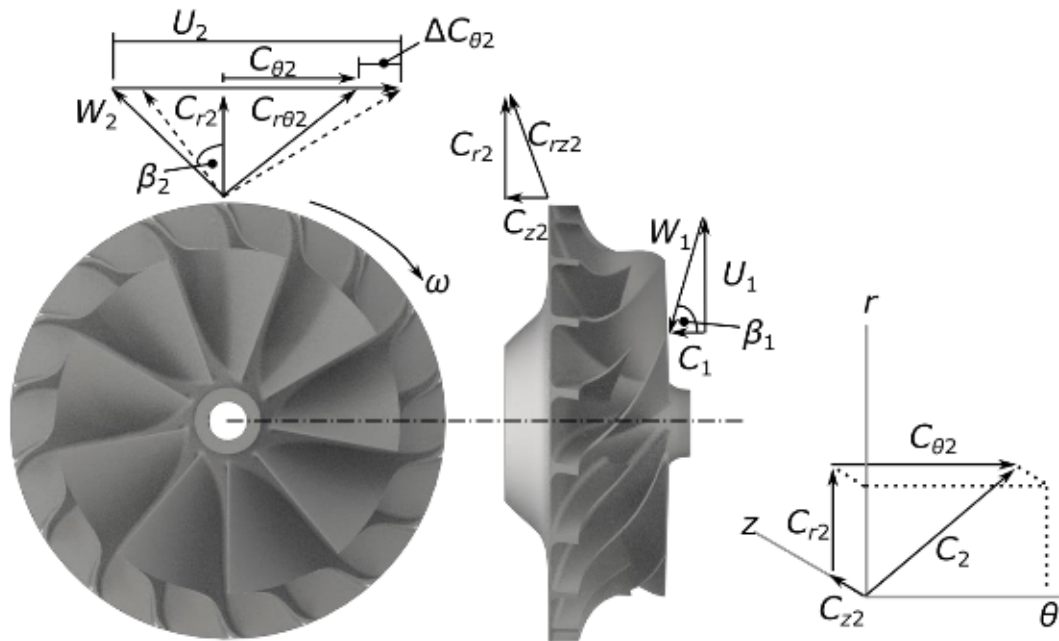


Figure 2.3: Mixed-Flow Compressor Impeller Velocity Triangles (Diener, 2016)

2.3 Basic Compressor Theory

The Mollier chart, presented in Figure 2.4, shows the operation of a compressor according to the enthalpy changes that take place throughout the different stages. The process between 0 and 1 is that of the inlet, 1 to 2 is that of the impeller and 2 to 3 is that of the diffuser. Stagnation conditions are denoted by a subscript 0 which appears before the subscript number indicating the state (or station). Single subscripts imply static conditions.

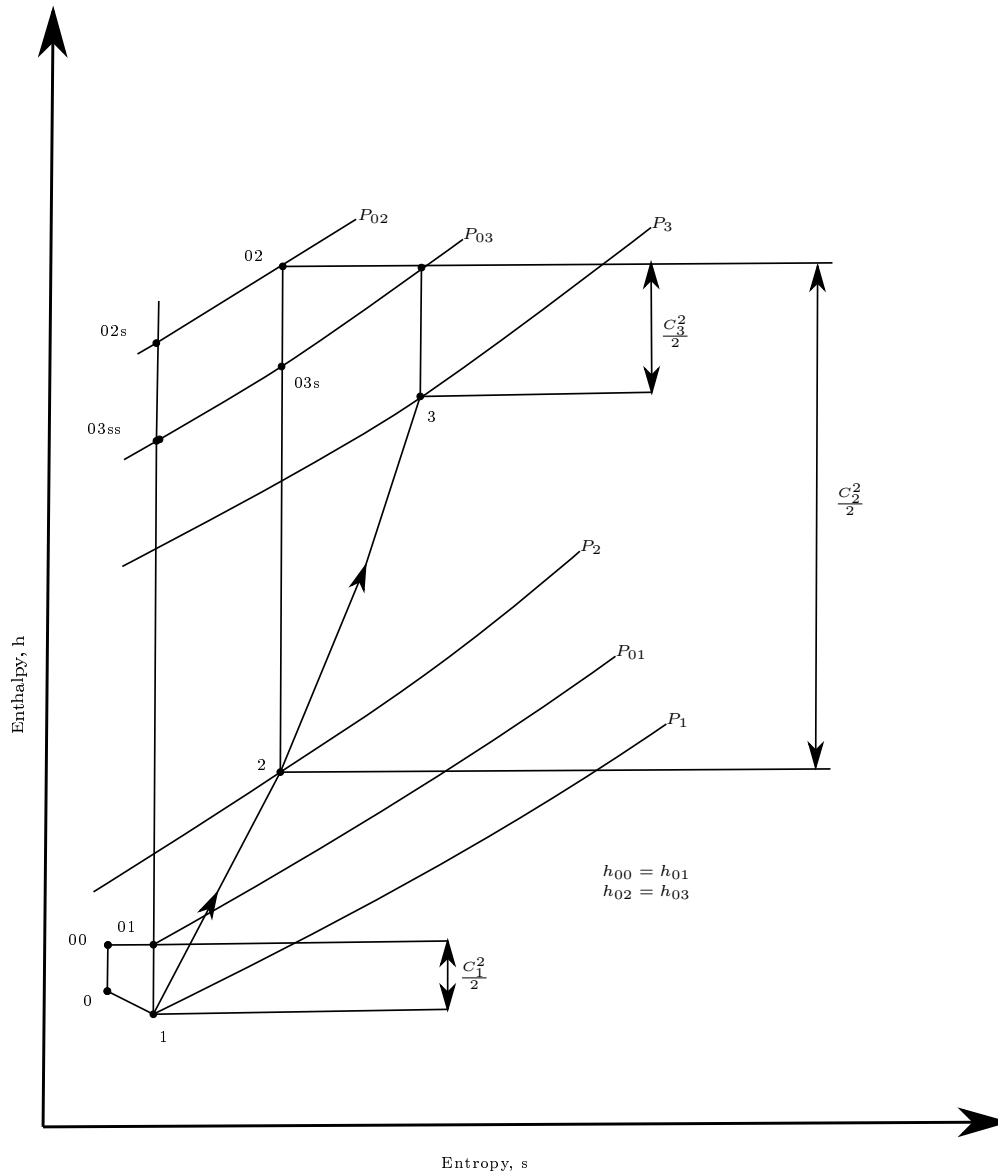


Figure 2.4: Mollier Chart for a Compressor

Work is done on the fluid between sections 1 and 2, thereby raising the total enthalpy. The rise in enthalpy is equal to the amount of work done by the impeller on the flow, W :

$$\Delta W = U_2 C_{\theta 2} - U_1 C_{\theta 1} = h_{02} - h_{01}. \quad (2.1)$$

When substituting $h_{0n} = h_n + \frac{C_n^2}{2}$ a function I , widely known as rothalpy, can be defined as:

$$I = h_1 + \frac{C_1^2}{2} - U_1 C_{\theta 1} = h_2 + \frac{C_2^2}{2} - U_2 C_{\theta 2}. \quad (2.2)$$

Rothalpy is a fluid mechanical property with relevance in the study of flow within rotating systems. It is a contraction of rotational stagnation enthalpy and remains constant through the impeller (Dixon and Hall, 2010). In terms of static enthalpy the rothalpy is given by:

$$I = h + \frac{1}{2}C^2 - UC_{\theta}. \quad (2.3)$$

After some manipulation of Equation (2.2) it can be shown that the static enthalpy rise between sections 1 and 2 is given by the following equation:

$$h_2 - h_1 = \frac{U_2^2 - U_1^2}{2} + \frac{W_1^2 - W_2^2}{2}. \quad (2.4)$$

The main contributor to the static enthalpy change in Equation (2.4) is the $\frac{1}{2}(U_2^2 - U_1^2)$ term, explaining why static enthalpy rise in a centrifugal compressor is so large compared to a single-stage axial compressor (Dixon and Hall, 2010).

2.4 Impeller Performance

The performance of a compressor impeller is defined according to the total-to-total pressure ratio:

$$\square_{imp(T-T)} = \frac{p_{02}}{p_{01}} \quad (2.5)$$

and the total-to-total isentropic efficiency:

$$\begin{aligned}
 \eta_{imp(T-T)} &= \frac{h_{02s} - h_{01s}}{h_{02} - h_{01}} \\
 &= \frac{\left(\frac{p_{02}}{p_{01}}\right)^{\frac{\gamma-1}{\gamma}} - 1}{\left(\frac{T_{02}}{T_{01}}\right) - 1}.
 \end{aligned} \tag{2.6}$$

Total-to-static values are often used if the exit kinetic energy is lost (Dixon and Hall, 2010). The impeller tip speed, U_2 , has a significant effect on the pressure ratio that an impeller can achieve. Material properties, however, limit the tip speed that can be attained, because the material stresses increase proportionally to the tip speed squared (Sandberg, 2016).

Figure 2.5 shows a typical compressor map of mass flow parameter $\frac{\dot{m}\sqrt{T_{01}}}{p_{01}}$ against pressure ratio. The point of maximum efficiency is indicated in the figure, along with the surge line, operating line and several corrected speed lines. Surge and choke (further discussed in Section 2.7) represent the two extremes of the impeller performance map, and stable operation of the compressor is achieved between these two extremes. The throat of an impeller is located at some point along a streamline through the rotor. If the flow reaches sonic velocity, $\text{Mach} \geq 1$, at the throat the flow through the compressor is said to choke (Dixon and Hall, 2010). When choke occurs no additional mass flow can pass through the compressor (Boyce, 2012). This region is identified by the rapid drop in pressure ratio with a minimal change in mass flow for a constant speed line. Surge occurs when the flow through the compressor becomes unstable. This instability is characterised by the main flow through a compressor reversing the direction of flow, during which the back (outlet) pressure drops and the main flow assumes its proper direction. This is followed by a rise in back pressure, causing the main flow to reverse again (Boyce, 2012).

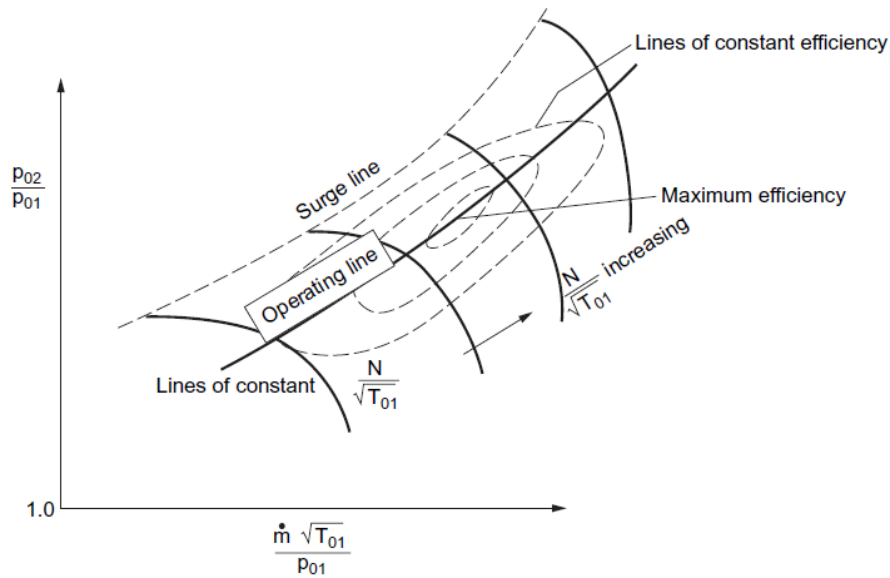


Figure 2.5: Overall Characteristic of a Compressor (Dixon, 1998)

2.5 Slip

Slip is a phenomenon in a centrifugal and mixed-flow turbomachine that reduces the absolute tangential velocity, $C_{\theta 2}$, of the working fluid at the outlet. Given that there is a finite number of blades, the relative velocity angle at the exit of the impeller β_2' is not equal to the exit angle of the blade, β_2 (Ji *et al.*, 2010) as shown in Figure 2.6.

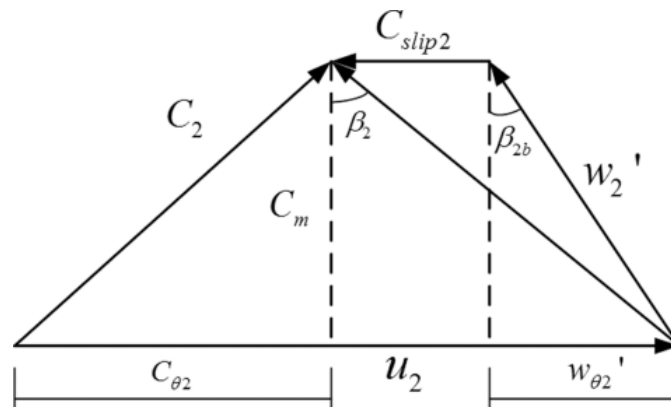


Figure 2.6: Velocity Triangle at the Outlet of a Backswept Impeller (Ji *et al.*, 2010)

Boyce (1993) mentions that the cause of the slip phenomenon within an impeller is not known exactly, but there are however general reasons that contribute to the change in the flow, namely:

Coriolis Circulation - Circulation of the working fluid within the rotor flow passage caused by the pressure gradient between the walls of two adjacent blades, the Coriolis force and the centrifugal force. This circulation causes a velocity gradient at the impeller exit that results in a net change in the exit flow angle. Figure 2.7 illustrates the Coriolis circulation in a centrifugal impeller. By changing the outlet angle from a radial direction (centrifugal impeller) to a mixed-flow configuration, the Coriolis force is relaxed and subsequently slip is reduced. The amount of change in the radius of the mean flow path as well as the amount of change in the meridional exit angle determines the degree to which the Coriolis force is relaxed (Diener, 2016).

Boundary layer Development - Within the impeller passages, a boundary layer develops that causes the fluid to experience a smaller exit area. The reduced area means the velocity must increase to satisfy continuity, which results in a higher relative exit velocity. Since the meridional velocity remains constant (see Figure 2.6), the absolute velocity must decrease, because of the increase in the relative velocity (W'_2 , which is the ideal velocity should the fluid follow the exact blade profile, becomes W_2 at an angle β_2 as opposed to β_{2b}).

Leakage - Fluid that flows through the tip gap from one side of a blade to the other side is referred to as leakage flow. Leakage reduces the amount of energy that is transferred from the impeller to the working fluid and thus results in a smaller exit velocity angle.

Number of Vanes - The number of vanes has a direct impact on the loading that the vane experiences. The higher the number of vanes, the lower the vane loading and the closer the fluid follows the vanes. When the vane loading is higher, the fluid tends to group on the pressure side of the blade and introduces a velocity gradient at the exit.

Vane Thickness - Due to physical necessity, vanes have a finite thickness. Once the fluid exits the impeller, the vanes no longer contain the flow and the meridional velocity is immediately reduced. Both the absolute and relative velocities decrease, which results in a change in the exit angle of the fluid (Boyce, 1993).

When designing centrifugal or mixed-flow impellers, designers need methods to

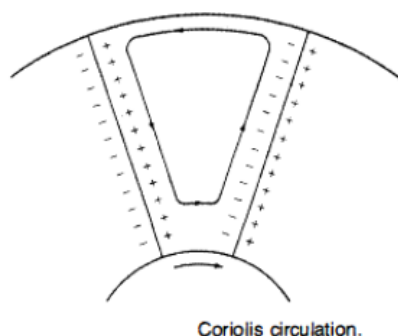


Figure 2.7: Coriolis Circulation in a Centrifugal Impeller

accurately predict impeller drive shaft torque and the energy input into the flow. Ji *et al.* (2010) states that "predicting slip factor for centrifugal impellers is at the core of turbomachinery meanline modeling." The slip factor influences the velocity triangle at the exit, the work input, and pressure rise. Slip factor is usually determined by the vorticity of the internal flow relative to the rotating impeller. The slip factor formulation by Stodola (1945) is one of the most common formulations used in textbooks, while there are many other authors with approximate slip factor predictions. Qiu *et al.* (2011) found that slip factor predictions by authors such as Stodola (1945), Wiesner (1967), and Eck (1973) typically work well for one series of impellers, while they performed worse or even failed (unrealistic results and/or unable to produce a result) for other types of impellers. Furthermore, tests have shown that the slip factor varies from design to off-design conditions (Qiu *et al.*, 2011). The implementation of slip factor in the 1-D mean-line code is further discussed in Section 3.7.1.

2.6 Splitter Blades

Cumpsty (1989) states that there must be an adequate number of blades at the exit of an impeller if the blade loading is to be kept within reasonable bounds. The problem with a larger number of blades is that the blockage at the inducer section of the impeller may impose a constraint on the mass flow in high pressure machines (Cumpsty, 1989). The expedient adopted is the use of splitter blades. They reduce the blade loading and potentially increase the mass flow capability at the throat of the inducer (Aungier, 2000; Cumpsty, 1989; Japikse, 1996). The splitter blade starts some length downstream of the inlet of the impeller and continues up until the exit of the impeller.

It is customary to design these splitter blades to be identical to the full blades,

but cut back. The impeller is manufactured with a full set of blades, with every other blade being cut back, forming the splitter blades. Cumpsty (1989) however notes that this is not the right procedure as the leading edge of the splitter blades will not align with the flow approaching it in the middle of the passage. Shroud pressure contours measured by Senoo *et al* (1979) show that the flow in the two passages divided by a splitter behave quite differently. Cumpsty further mentions that there are many potential outcomes with both axial and radial variation in the leading edge of a splitter blade.

2.7 Compressor Instabilities

Compressor instabilities are attributed to flow phenomena. These flow phenomena include stall, surge and choke.

Stall

Rotating stall, also known as propagating stall, consists of regions of stall covering the blade passages and propagates in the direction opposite of the rotor's rotation (shown in Figure 2.8) and at some fraction of rotor speed (Boyce, 1993). Cumpsty (1989) states that rotating stall is a mechanism whereby the compressor adapts to a mass flow which is too small. Instead of trying to share the flow over the entire annulus the flow is shared unequally so that some blade passages have a larger flow than others. Boyce (1993) notes that the number of stall regions and the propagation rates vary considerably. Ignoring surge, the stall region of a compressor defines the lowest possible working mass flow rate of the compressor.

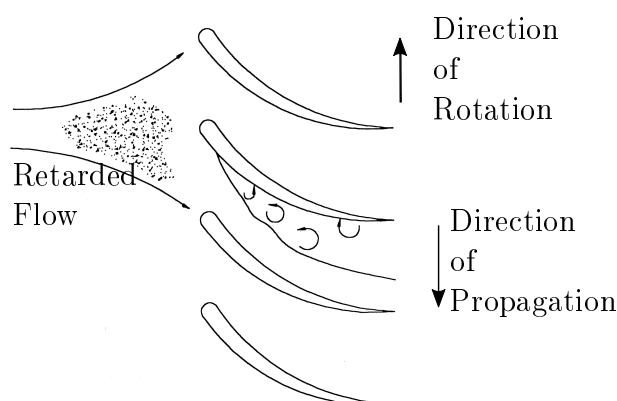


Figure 2.8: Rotating Stall in a Centrifugal Compressor Inducer (Boyce, 1993)

Surge

Surge is an unstable condition that results in the reversal of flow and pressure fluctuations in the system (Boyce, 1993). Boyce also states that an excessive increase in the resistance of a system while operating at a specific speed will result in surge. The result of the added resistance is an instability in the flow. Surge can also take place when the resistance remains unchanged, but the speed is reduced considerably. Surge thus depends on the type of system and the shape of the resistance curve (Boyce, 1993). The resistance curve is a line representing the process resistance of the compressor and the steady state operating point of the compressor is usually found where the resistance curve intersects the line of constant speed (Mirsky *et al.*, 2013). The shape of the resistance curve thus depends on the process resistance of the system.

Choke

The throat areas of a compressor stage are the regions in the compressor where the internal flow area is a minimum along a streamline. If the Mach number reaches unity at the throat area, the mass flow is at a maximum, and the flow is said to be choked (Diener, 2016). In comparison to the stall region, the choke region of a compressor defines the highest possible working mass flow rate that the compressor can attain.

Chapter 3

Mean-Line Code

This chapter details the 1-D mean-line code developed by De Wet (2011) in order to give the reader an understanding of how the code works. The proposed changes to be made to the code to allow the performance analysis of both centrifugal and mixed-flow impellers are also discussed in this chapter.

3.1 Introduction

The one-dimensional mean-line code is an in-house code, written in Matlab[®], that was first developed by De Wet (2011), based on the procedure as developed by Aungier (2000). Aungier allows for the definition of component sizing, geometry definition and performance of the compressor. The design process consists of: 1) the meridional passage design, 2) detailed blade design, 3) component sizing, 4) and performance analysis. The user defines the total thermodynamic conditions and angular momentum for the inlet conditions.

Later versions of the code allow for optimisation and therefore the design of an impeller according to user-defined design parameters. The code can also be applied for analysis of a single geometry by specifying the design parameters as non-varying parameters. By doing this the "optimisation" of a geometry within specific design boundaries is eliminated, and instead, a single geometry is created according to the user-defined geometry specifications. Although the mean-line code was used for analysis only (of existing impellers) in this thesis, both the structure and functions of the code are described in this chapter for continuity.

3.2 Code Structure

The mean-line code was initially developed to predict the performance of centrifugal compressors. Subsequent authors of follow up research projects added to the original code to enable it to analyse diffusers as well. This research project aimed to adapt the code to allow for the analysis of a mixed-flow impeller in addition to a radial flow impeller. The mean-line code generates a *geomTurbo* output file (containing the three-dimensional impeller geometry) which can be uploaded directly into Numeca AutoGrid5™ to start the CFD validation and optimisation process.

The mean-line code is executed from one main function. The main function, *optimise*, makes use of a genetic algorithm (Van der Merwe, 2012) to create the best performing impeller according to the performance criteria and geometrical constraints. The optimisation process is executed for a user-defined number of optimisation steps. It should be noted that the number of optimisation steps should be increased as the number of free parameters is increased. The development of the impeller geometry and performance analysis are executed within a loop, according to the number of chromosomes specified by the user. This loop is repeated for each optimisation step.

The first step is to create an impeller geometry and calculate a blade throat area according to the specific geometry. Once the geometry is created and the throat area is known, the performance of the impeller can be determined. When the optimisation steps are finished, the best possible impeller for the specified geometrical limits is created, upon which the performance of the compressor is determined at different rotational speeds. Van der Merwe (2012) added the creation of a performance map for the compressor at different operational speeds. A flow diagram showing the logic for the mean-line code structure is shown in Figure B.1.

3.3 Code Inputs

The code, in its intended format, consists of several functions that are used to determine the performance of the impeller and then create a geometry based on the parameters that deliver the best performance. The main geometric and operating properties of the compressor are specified in the main function called *optimise*. These parameters can vary and are subsequently given a range of possible values. The free geometric parameters for the Van der Merwe (2012) mean-line rotor, with their bounds are given in Table 3.1.

The main function generates a compressor geometry based on the main parameters

Table 3.1: Free Parameters of Van der Merwe (2012) Rotor

Parameter	Value
β_{1H}	[50 70]
β_{1S}	[20 35]
β_2	[60 90]
K_3	[1 5]
K_4	[1 5]

that were specified. An example of the main parameters required to create the geometry of the k27 impeller is shown in Table 3.2. The main geometrical parameters for all other impellers analysed with the mean-line code are shown in Appendix A. The mean-line code uses the same boundary conditions as specified for the CFD simulation. Total quantities are imposed at the inlet as atmospheric conditions ($T_{01} = 293K$ and $p_{01} = 101.325kPa$), while the inlet velocity is specified in the axial direction (z -direction). A performance function is used to calculate the performance of the compressor based on a surge margin mass flow rate and a normal (operational) mass flow rate. The results of these are then used as mass flow rate weighting factors in the calculation of the objective function. Once the optimisation process is completed and a final compressor geometry has been calculated, a compressor chart is created that displays the performance of the compressor at different rotational speeds. Flow diagrams showing the logic for the performance and display chart Matlab[®] scripts are shown in Appendix B.

3.4 Impeller Geometry

The mean-line geometry is used as input for a mean-line CFD simulation, after which improvement updates to the geometry are made. The mean-line geometry has to adhere to specific dimensional bounds and a specific format in order to be exported as a CFD geometry file (for Numeca software, this is referred to as a *geomTurbo* file). The required geometry included meridional contours of the hub and shroud, the camber line of the main and splitter blades, the blade thickness distribution, and the number of blades.

It is important to note here that changes to code regarding the geometry configuration of the impeller, centrifugal or mixed-flow, has already been made by Diener (2016) in an attempt to adapt the code to be suitable for mixed-flow impellers. The mean-line code, therefore, already allows for a mixed-flow geometry to be created.

Table 3.2: K27 Main Parameters

Parameter	Value
r_{1hub}	10.113 mm
$r_{1shroud}$	25.522 mm
r_2	40.439 mm
b_{imp}	28.814 mm
z_{imp}	7
β_{1hub}	58°
$\beta_{1shroud}$	30°
β_2	57°
θ_{1hub}	5°
$\theta_{2shroud}$	10°
LE_{hub}	1.52 mm
LE_{shroud}	0.817 mm
TE	0.488 mm
CL	0.45 mm

3.4.1 Endwalls

The hub and shroud contours are the first to be created, by using straight lines as well as Bézier curves. The contours, consisting of an inlet, bladed, and diffuser section, are created in the meridional plane. The Bézier curves are used for the shroud wall of the diffuser as well as for the bladed section, while straight lines are employed for the rest of the endwall contours. Bézier curves are a general method used to generate smooth curves that are suitable for gas path design (Aungier, 2000).

Figure 3.1 shows the Bézier control points and endwall contours in the meridional plane. The Bézier curves defining the impeller endwalls consist of four control points each, defined by a r and z coordinate in the meridional plane. A vaneless diffuser is added to the geometry to form a complete computational domain. The diffuser acts as a guide to direct the flow to the outlet of the computational domain. The vaneless diffuser consists of straight walls for the hub and shroud, with a pinch added at the outlet of the flow domain. The radius of the diffuser outlet is given by:

$$r_3 = 1.5r_2. \quad (3.1)$$

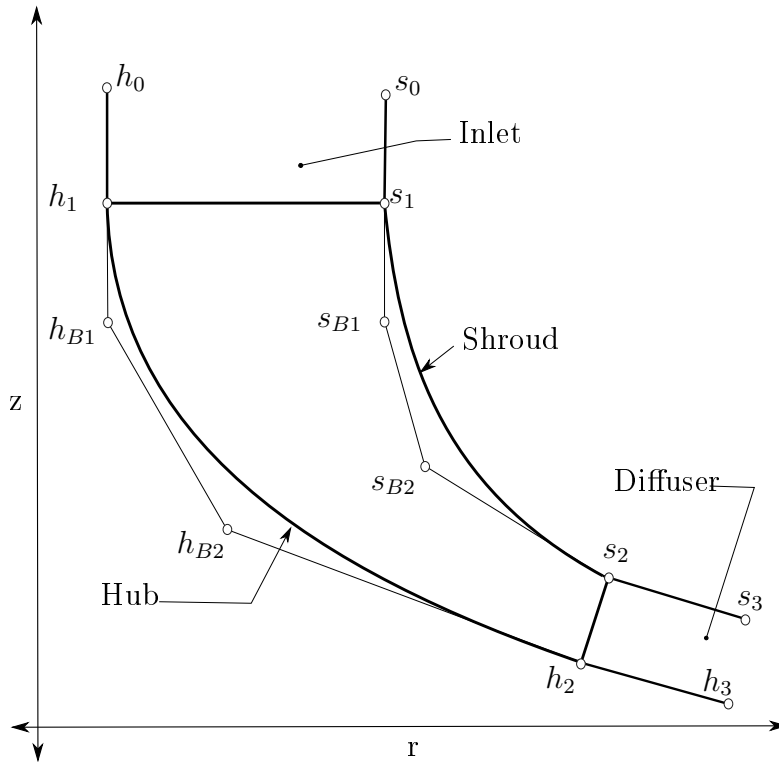


Figure 3.1: Meridional View of Endwall Contours and Bézier Control Points

3.4.2 Blades

The blades make up the most complex geometric feature of the compressor. The blade of a compressor is defined by several parameters, of which the number is determined by the complexity of the blade. The blades in this project are defined by its meridional hub and shroud contours first, after which the camber line is defined in the $dm/r-\theta$ plane. Figure 3.2 shows the definition of the blade camber line. The distribution of the angle $\beta(u_m)$ at any point on the hub or shroud contour defines the blade camber lines. A third order polynomial (Verstraete *et al.*, 2010) given in equation Equation (3.2), is used to define the distribution of $\beta(u_m)$ at the hub and shroud:

$$\beta(u_m) = \beta_0(1 - u_m)^3 + 3\beta_1u_m(1 - u_m)^2 + 3\beta_2u_m^2(1 - u_m) + \beta_3u_m^3. \quad (3.2)$$

The position u_m is the non-dimensionalised meridional length ($u_m \in [0,1]$, 0 at the leading edge, and 1 at the trailing edge). β_0 and β_3 represents angles at the leading edge and trailing edges respectively of the blade. The camber line circumferential

position, θ , is then defined by:

$$rd\theta = dm \tan \beta \quad (3.3)$$

where r equals the radial coordinate of a point on the camber line and dm equals the length of a finite camber line section in the meridional plane.

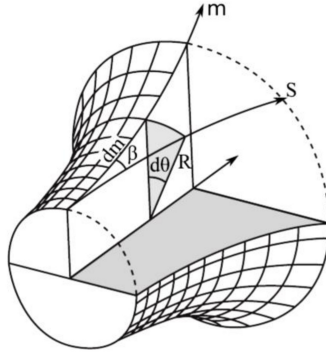


Figure 3.2: Definition of the Blade Camber Line by β angle (Verstraete *et al.*, 2010)

The main blade profile is created by using equations (3.2) and (3.3). The creation of the splitter blades is then simple, as the same blade profiles from the main blade are used. The splitter blade is essentially just a fraction of the main blade. To define the splitter blade, the hub and shroud contours of the main blade are cut off at a predefined length. The fraction, $f_{startsplit}$, is used to set the length of the splitter blade as shown in Equation (3.4).

$$L_{CL_{split}} = L_{CL_{main}} \times f_{startsplit} \quad (3.4)$$

A single fractional value is used for both the hub and shroud camber lines, although Van der Merwe (2012) investigated the use of independent values. The circumferential position of the camber line, θ , of the splitter blades are defined by:

$$\theta_{split} = \theta_{main} - \frac{360}{2z_{main}} \quad (3.5)$$

where θ is given in degrees and z_{main} refers to the number of main blades on the impeller.

Verstraete *et al.*'s (2010) procedure for defining blade thickness was followed. Figure 3.3 shows a schematic for the thickness distribution of the blades, consisting of elliptical, constant, and parabolic sections. The distribution of the different sections is defined as a function of the nondimensionalised camber length, u .

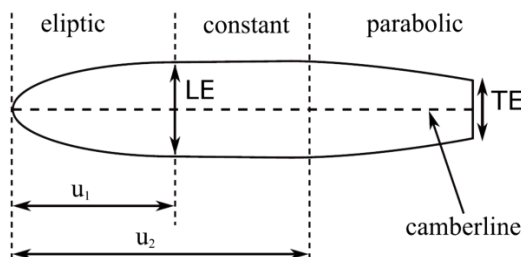


Figure 3.3: Blade Thickness Distribution Normal to the Camber Line (not to scale) (Verstraete *et al.*, 2010)

The values for the different parameters of Figure 3.3 are given in Table 3.3. The trailing edge thickness, TE , was calculated to have a value that is 10% of the trailing edge blade height.

Table 3.3: Thickness Distribution Parameters for the k27 Impeller

Parameter	Value
u_1	0.1
u_2	0.8
LE_{hub}	1.52
LE_{shroud}	0.817
TE	0.488

The mean-line code also allows for a blade lean angle to be defined. A default angle of 90° is used in this project. In the case of defining a blade lean angle, an option exists to extend the shroud trailing edge to ensure that the blade edge at the tip is normal to the flow direction. This is achieved by increasing the variable r_{tip_shroud} .

The clearance gap, CL , also known as the *tip gap*, is the last parameter to be assigned. The clearance gap is the gap between the blades and the shroud. When

assigning the clearance gap size, it is important to consider the operation of the impeller at full speed. Centrifugal- and heat-expansion forces are significant contributors to the blades expanding and require sufficient space to maintain a gap for safe operation. A clearance gap, constant along the length of the blade, was calculated using the following relation from Zemp *et al.* (2010):

$$\frac{CL}{b_2} = 4.5\%. \quad (3.6)$$

3.5 Impeller Performance

As mentioned in Section 3.3, the performance of the impeller is evaluated according to pressure ratio and isentropic efficiency at the outlet of the impeller. An objective function is used to weigh the pressure ratios and efficiencies for the different geometries throughout the optimisation process. This then allows the performance of the impeller to be evaluated as a single value, given by:

$$P = \frac{\Pi_{t-t}}{5} + \frac{\eta_{t-t}}{0.8}. \quad (3.7)$$

The target values for pressure ratio and efficiency for the respective impellers are used as weighting factors in Equation (3.7). Table 3.4 shows the target values for the respective impellers. The objective function target value is therefore 2. A value higher than two would indicate better performance than the target performance, and a value below two would indicate weaker performance. The performance of each iteration geometry within the optimisation process is evaluated through a function calculating the pressure ratio and efficiency according to the specified geometry. The performance of each iteration is then compared to the previous one, where the impeller with the best performance is then saved as the "best" performing impeller. This process continues until all the possible geometries are evaluated (Van der Merwe, 2012)

Table 3.4: Target Values for Respective Impellers

Impeller	Target Values	
	\square	η
k27	4.5	0.85
Van der Merwe	5	0.9
Diener	5	0.85

3.6 Code Output

The code generates several figures, showing the hub and shroud Bézier endwalls, along with a 3-D figure showing the hub and shroud curves with the blades. The complete geometry created by the code is written to a CFD geometry file format, while all the contours are written to separate text files. Finally, a compressor performance map is created, showing the pressure ratio and efficiency curves for the impeller at different operating speeds. Included in the performance maps is a surge line based on the surge condition specified by the user. The compressor maps for each impeller analysed in the mean-line code are shown in Appendix D.

3.7 Adjustment of the In-House Code

This section outlines the steps followed in order to successfully modify the in-house mean-line code to analyse mixed-flow impellers.

3.7.1 Slip Formulation

The pressure rise in a compressor is supplied by the useful work input of the impeller blades. Impeller work input is essentially the total enthalpy rise imparted to the fluid by the impeller. When the fluid entering an impeller is considered to be irrotational, a relative eddy rotating in the opposite direction of the rotor direction is required to maintain the irrotational flow in the absolute frame of reference. This is the main contributor to slip that exists at the impeller outlet (Dixon, 1998; Ji *et al.*, 2010; Qiu *et al.*, 2011).

Slip reduces the effective work of an impeller on the working fluid passing through a compressor. Predicting the amount of slip that occurs for a given impeller is therefore important to correctly determine the performance of an impeller. Over the years many authors have proposed different correlations for slip factor in order

to quantify the effective/real flow as opposed to the ideal flow at impeller outlet. It should be mentioned though that most slip factor correlations are derived for centrifugal impellers only or blades with no sweep.

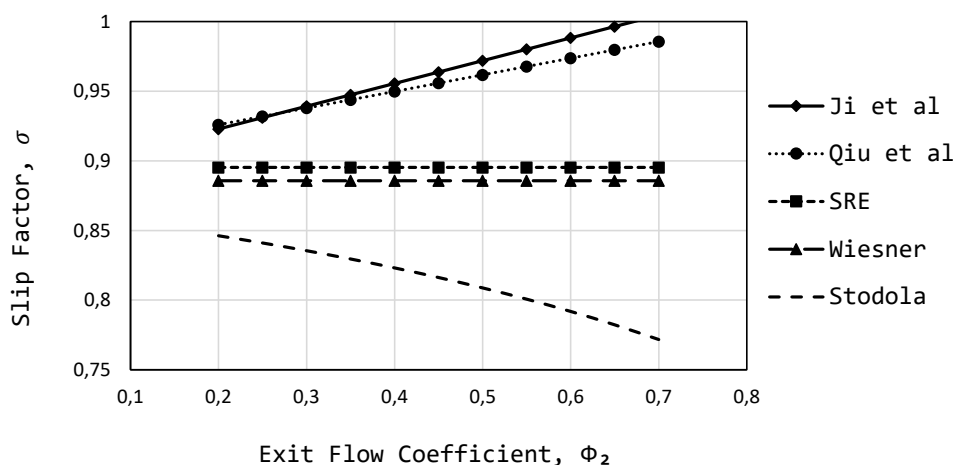
Busemann (1928) was one of the first researchers to publish a method by which the slip in radial flow impellers could be predicted. Busemann (1928) derived his method by analysis of the flow field between logarithmic spiral blades. Most studies, however, prefer to use the curves published by Wislicenus (1965), due to the extensive mathematical treatment required to use the Busemann method. Wiesner (1967) also derived an equation for the prediction of slip, but he based his equation on the analysis of a large number of empirical results. Stodola (1945) presented a simplified derivation of slip that is followed by many textbooks. The formulation by Stodola makes use of the relative eddy mechanism, often considered as the most important mechanism for slip. Stodola describes the relative eddy as a circle, inserted between the blade passages near the outer radius of the rotor. The circle, with a vorticity of ω , touches the suction side trailing edge of one blade and is tangent to the pressure side of the neighbouring blade. The slip velocity is then given by $\Delta w = \pi \Omega r_e (\cos \beta) / Z$.

Many more researchers like Stanitz (1952), Eck (1973), Pampreen and Musgrave (1978), Pfeleiderer (1961), Visser *et al.* (1994), and Paeng and Chung (2001) proposed their own estimations for slip. This thesis specifically considers slip formulations by the following authors: Ji *et al.* (2010), Von Backström (2006), and Qiu *et al.* (2011). These authors developed formulations for slip factor which are valid for both centrifugal and mixed-flow compressor impellers. Diener (2016) employed the Wiesner (1967) slip formulation in the 1-D mean-line code, but the code did not sufficiently predict the performance of a mixed-flow impeller. It should be noted that the slip formulation according to Wiesner (1967) does not take the meridional outlet angle into account. It, therefore, does not cater for the axial flow element in the working fluid leaving the impeller. Ji *et al.* (2010) and Qiu *et al.* (2011) accommodates mixed-flow impellers by incorporating the meridional exit angle, α_{c2} , in their formulation of the slip factor. Table 3.5 shows the main geometrical parameters for the Eckardt Rotor 'A', while Figure 3.4 shows the differences in slip factor according to different authors for the Eckardt Rotor 'A' impeller.

Table 3.5: Main Geometrical Parameters for the Eckardt Rotor 'A'

Parameter	Value
r_2	200 mm
b_{imp}	130 mm
z_{imp}	20
β_{a2}	60°
α_{c2}	90°

A large deviation between Stodola's slip factor and that of the other authors is visible. Von Backström's (2006) SRE method and Wiesner's (1967) slip factor compare well, while Ji *et al.*'s (2010) and Qiu *et al.*'s (2011) slip formulations record the largest values for the Eckardt Rotor A. The three slip factor correlations under consideration are discussed next.

**Figure 3.4:** Various Slip Factors for Eckardt's Rotor 'A'

Ji et al Slip Factor Correlation

Ji *et al.* (2010) derived their slip formulation on the basis of the Euler equation in turbomachinery and the relative eddy theory of Stodola. Their slip formulation is both a function of geometric parameters as well as flow coefficient, allowing the slip factor to vary with varying flow rate. Ji *et al.*'s (2010) slip factor is given by:

$$\begin{aligned}
\sigma &= 1 - \frac{C_{slip2}}{u_2} \\
&= 1 - \frac{F\pi}{2Z + F\pi \sin\alpha_{c2}} \\
&\quad \left[(2 + \phi_2 \tan\beta_2) \sin\alpha_{c2} + \frac{\phi r_2}{\cos^2\beta_{2b}} + \frac{d\beta_b}{dm} \Big|_2 \right]
\end{aligned} \tag{3.8}$$

where F is the shape factor given by,

$$F = \frac{Z}{\pi} \sin\left(\frac{\pi}{Z}\right) \cos\left(|\beta_{2b}| - \frac{\pi}{Z}\right) - \frac{t_2}{s_2 \cos\beta_{2b}}. \tag{3.9}$$

According to Equation (3.8) the slip velocity is affected not only by the common parameters such as blade angle, meridional inclination angle and blade number but also by the flow coefficient ϕ_2 and the blade angle turning rate $(d\beta/dm|_2)$. The radius ratio is indirectly included in the formulation, by influencing the blade angle turning rate. Ji *et al.* (2010) validated their new correlation by testing it on a variety of impeller cases, including mixed-flow impellers. They compared their results to those calculated by Stodola (1945), Stanitz (1952), Wiesner (1967), Busemann (1928), and Paeng and Chung (2001) and also to experimental results. Table 3.6 shows their findings, along with the main geometrical parameters for each impeller. The error given in percentage is the difference between the slip factor according to the Ji *et al.* (2010) correlation and that calculated experimentally.

Table 3.6: Ji *et al.* Slip Factor Results. Adapted from Ji *et al.* (2010)

	R1-6A	R1-5A	R1-1	R1-4A	Rotor 'O'
r_2 (mm)	81	81	81	85	200
z_{imp}	4	5	6	8+8	20
β_{2b} (degree)	25.5	25.5	25.5	69.3	90
α_{c2} (degree)	45	45	45	45	90
σ - Stodola	0.660	0.730	0.775	0.816	0.843
σ - Stanitz	0.505	0.604	0.670	0.877	0.901
σ - Wiesner	0.743	0.786	0.812	0.861	0.877
σ - Busemann	0.692	0.745	0.772	0.860	0.875
σ - Paeng	0.782	0.819	0.844	0.868	0.884
σ - experiment	0.721	0.768	0.829	0.832	0.880
σ - Ji <i>et al.</i>	0.753	0.805	0.836	0.871	0.872
Error (%)	+4.44	+4.82	+0.84	+4.69	-0.09

SRE Slip Factor Correlation

Von Backström (2006) developed a slip correlation based on a fluid element in the rotor that rotates around the axis of the machine, instead of rotating around its own axis, as proposed by Stodola (1945). There is therefore only a single relative eddy in the rotor and not one in each blade passage. The single relative eddy of Von Backström also rotates with the same angular velocity of the rotor and in the opposite direction of the rotor. The SRE (Single Relative Eddy) slip factor by Von Backström is given by:

$$\begin{aligned}\sigma_s &= 1 - \frac{1}{1 + F(c/s_e)} \\ &= 1 - \frac{1}{1 + 5(c/s_e)(\cos\beta)^{0.5}}\end{aligned}\quad (3.10)$$

where F , the solidity influence coefficient, is equal to $F = F_0(\cos\beta)^{0.5}$, or in terms of the basic parameters:

$$\sigma_s = 1 - 1 / \left(1 + 5 \frac{(1 - RR)Z}{2\pi(\cos\beta)^{0.5}} \right). \quad (3.11)$$

Von Backström's slip correlation does however not make provision for a change in

the flow rate, but it does directly accommodate the radius ratio. Von Backström (2006) compared his results to that of Stodola (1945), Stanitz (1952), Wiesner (1967), and Busemann (1928) as presented in Table 3.7. The asterisk (*) denotes values corrected for exceeding Wiesner's limiting radius ratio, RR_{lim} , given by:

$$RR_{lim} = \exp[8.16(\cos\beta)/z]. \quad (3.12)$$

Table 3.7: SRE Slip Factors Compared to Predictions by other Authors, for $RR=0.5$ and $\beta = 50^\circ$.

Z	4	8	16
Stodola	0.495	0.748	0.874
Wiesner	0.676*	813	0.885
Busemann	0.63	0.79	0.88
SRE	0.665	0.799	0.888
Stanitz, $\beta = 0^\circ$	0.706	0.828	0.906
SRE, $\beta = 0^\circ$	0.614	0.761	0.864

Qiu et al Slip Factor Correlation

Qiu *et al.* (2011) proposed a formulation for the prediction of slip, that similar to Ji *et al.* (2010), makes provision for the change in flow rate and the change in the turning rate of the blade angle. Qiu *et al.* (2011) mentions that tests have proven that the slip factor varies from design to off-design conditions and that a dilemma arises when a mixed-flow compressor is considered. This is because a deviation angle is used in the case of axial cascades and the slip factor in the case of centrifugal impellers, raising the question whether the slip factor or the deviation angle should be used. Qiu *et al.* (2011) therefore aimed to address these two questions in formulating a new slip factor model that allows for off-design conditions as well as for mixed-flow impellers. Qiu *et al.*'s (2011) slip factor is given by:

$$\begin{aligned}
\sigma &= 1 - \frac{C_{slip}}{U_2} \\
&= 1 - \frac{F\pi\cos\beta_{2b}\sin\alpha_{c2}}{Z_2} - \frac{Fs_2\phi_2}{4\cos\beta_{2b}} \left(\frac{d\beta}{dm} \right)_2 \\
&\quad + \frac{F\phi_2s_2\sin\beta_{2b}}{4\rho_2b_2} \left(\frac{d\rho b}{dm} \right)_2
\end{aligned} \tag{3.13}$$

where the shape factor F is given by:

$$\begin{aligned}
F &= 1 - 2\sin\left(\frac{\pi}{Z_2}\right)\sin\left(\frac{\pi}{Z_2} + \beta_{2b}\right)\cos(\beta_{2b})\sin\alpha_{c2} \\
&\quad - \frac{t_2}{s_2\cos\beta_{2b}}.
\end{aligned} \tag{3.14}$$

Equation (3.13) can be split into three parts:

$$\sigma = 1 - \Delta\sigma_{radial} - \Delta\sigma_{turn} - \Delta\sigma_{passage}. \tag{3.15}$$

where $\Delta\sigma_{radial}$ is equal to the first term and is the decrement due to the rotational effect, $\Delta\sigma_{turn}$ is equal to the second term and is the decrement due to blade turning and $\Delta\sigma_{passage}$ is the last term in Equation (3.13) and is the decrement due to the passage width variation in the impeller. The introduction of the meridional outlet angle, α_{c2} , in the first term of Equation (3.13) allows the model to be applied to mixed-flow impellers as well.

Figure 3.5 shows the slip factor according to Phleiderer's definition ($\mu = \frac{C_{\theta 2}}{C'_{\theta 2}}$) of the Eckardt Rotor A for the three authors of interest. The same upward trend is visible for all three authors' slip factor correlation, although Von Backström slip factor is slightly lower than that of Ji *et al.* and Qiu *et al.*.

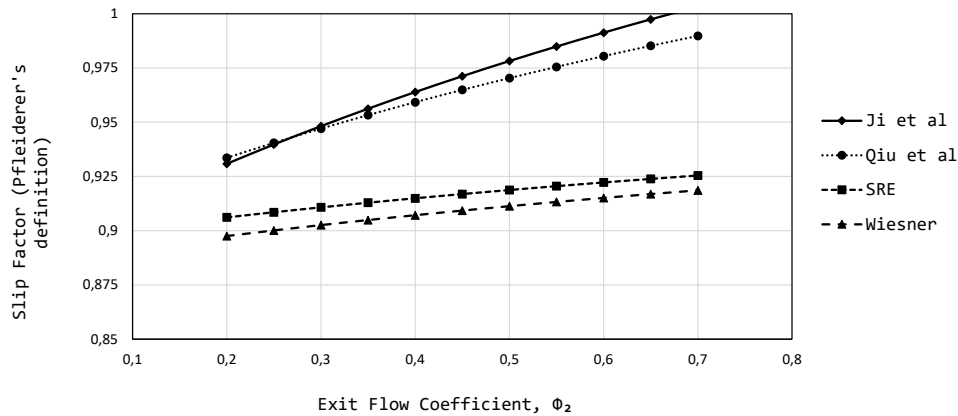


Figure 3.5: Different Slip Factors (Pfleiderer's definition) for the Eckardt Rotor A

The slip factor prediction for the k27 rotor is shown in Figure 3.6.

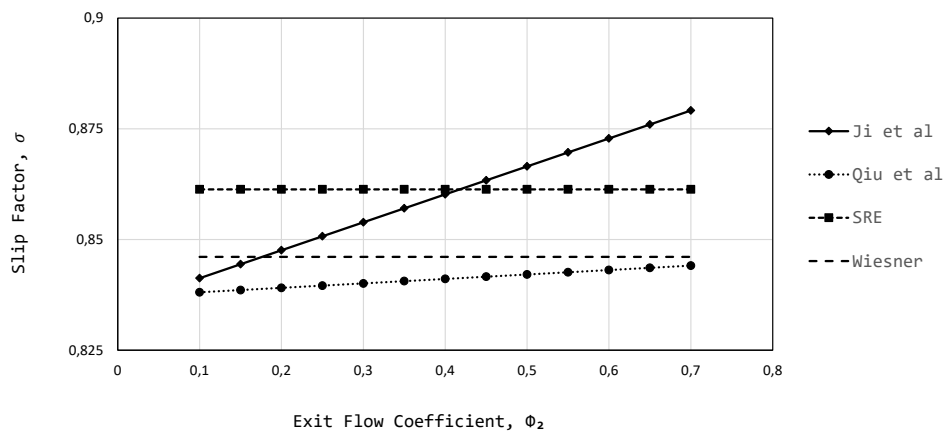


Figure 3.6: Different Slip Factors for the k27 Rotor

Ji *et al.*'s (2010) slip formulation was selected to replace the Wiesner slip factor model in the 1-D mean-line in-house code. Ji *et al.*'s (2010) slip factor model was preferred over Qiu *et al.*'s (2011) slip factor model, because it is simpler to implement and shown to give reliable results for both centrifugal and mixed-flow impellers. The largest deviation recorded compared to experimental results for different rotors was just below 5% (see Table 3.6).

3.7.2 Throat Area

Aungier (2000) states that "an accurate throat area calculation is critical to the aerodynamic design process." Besides the obvious role of establishing the choke flow limit for the rotor, the throat area is used to determine the impeller stall limit. The throat area is also employed in several of the loss models used in predicting the performance of the impeller. Aungier (2000) outlines a procedure for determining the blade passage throat area.

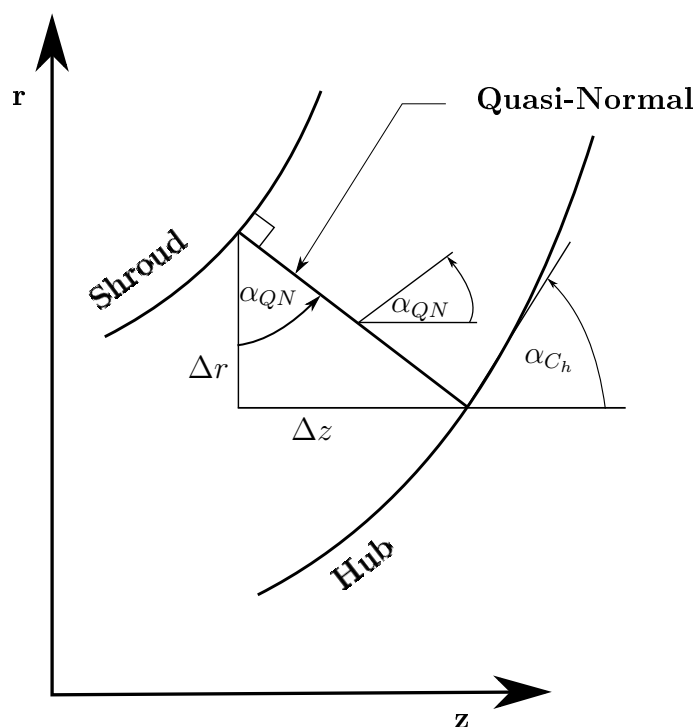


Figure 3.7: Quasi-Normal Geometry

In order to successfully determine the blade passage throat area, the blade-to-blade throat width and the distance along quasi-normals at the throat width location should be calculated. Figure 3.7 shows both a quasi-normal line along with the quasi-normal angles. Computing the blade-to-blade throat width is the most complicated step in the process of calculating the blade passage throat area, as the throat width, h_t , lies on a three-dimensional surface with both r and θ varying across the passage. Aungier (2000) suggests using conformal transformation in order to map the (m, θ) plane into a Cartesian plane (X, Y) . The suggested conformal transformation is path independent and can mathematically be expressed as:

$$X = \int_{m_1}^m \frac{dm}{r} \quad (3.16)$$

$$Y = \theta.$$

The contour "cone" angles and quasi-normal angles in Figure 3.7 are given by:

$$\sin(\alpha_C) = \frac{\partial r}{\partial m} \quad (3.17)$$

$$\tan(\alpha_{QN}) = \frac{\Delta z}{\Delta r}. \quad (3.18)$$

The throat width in the transformed coordinate plane is shown in Figure 3.8, which also illustrates that the throat width has a constant angle over its length. Angles are preserved in a conformal transformation and can mathematically be expressed as:

$$\frac{\partial Y}{\partial X} = \frac{r \partial \theta}{\partial m} = \text{constant}. \quad (3.19)$$

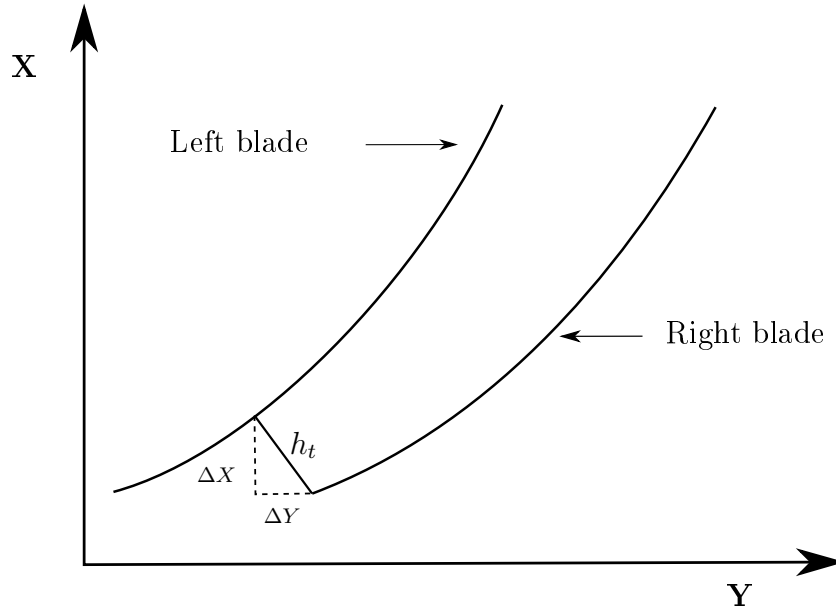


Figure 3.8: Throat in Transformed Plane

Since the angle given by Equation (3.19) remains constant along h_t , the throat width can be calculated as:

$$h_t = \int_{m_1}^m \sqrt{1 + \left(\frac{r\partial\theta}{\partial m}\right)^2} dm = \sqrt{1 + \left(\frac{\Delta\theta}{X}\right)^2} \Delta m \quad (3.20)$$

where $\Delta\theta$ and Δm are differences in values between points on the opposing blade surfaces, while X is evaluated on the left blade surface of Figure 3.8. Since Equation (3.20) can be applied to compute the distance between any two points on the opposing blade surfaces, it is used to compute the distances for all points on the left blade surface in Figure 3.8 from the fixed point on the right-hand surface. The minimum distance then represents the throat width on the particular stream surface. In order to correctly locate the throat width, the distribution of computed values can be differentiated numerically, and the result interpolated for a derivative of zero. If n is the distance along quasi-normals (see Figure 3.7) and $\epsilon = \alpha_{QN} - \alpha_C$, the blade passage throat area can then be estimated by:

$$\Delta A_t = \overline{h_t \cos \epsilon \Delta n} \quad (3.21)$$

where an average value for h_t on the two stream surfaces (hub and shroud) and

an average of $\Delta n \cos(\epsilon)$ on the opposing blade surfaces are used. To account for the fact that the quasi-normal may not be normal to the stream surfaces, $\cos(\epsilon)$ is used in Equation (3.21).

The original version of the mean-line code assumes that the throat of the impeller (where choke occurs) is located between the main blades of the impeller. It was however found that choke may take place between the main blade and splitter blade of the k27 impeller, raising the question whether the throat area of an impeller might be further downstream of the inlet. This led to the adaptation of the mean-line code throat area in order to calculate the throat parameters for the case of the throat being located between a main blade and splitter blade.

The change in the passage flow area, due to a change in the prediction of the throat area, necessitates a change in the amount of fluid flow through the throat area. This was achieved by the introduction of a new parameter that adapts the amount of flow by a factor equal to the newly predicted throat area over the originally predicted throat area. For the mean-line script that determines the design point of the impeller, this parameter is only used once in the throat conditions for-loop. In the script that determines the performance of the impeller for several impeller rotational speeds, this parameter is both employed in the throat conditions for-loop and in the for-loop determining the overall performance of the impeller. Flow diagrams for the main-, performance-, and display scripts are given in Appendix B.

The passage area ratio, A_R , is another variable that is influenced by the change in the throat area (Equation (3.22)). A_R is effectively the ratio of the impeller tip flow area to the throat area. It is formulated in such a manner that it permits analysts to make adjustments to the throat area in order to match performance predictions to an experimentally observed impeller choke limit without having an undesired effect on the work input prediction (Aungier, 2000). With the change in the throat area prediction, the minimum throat area may move down from the inlet of the impeller to the start of the splitter blade. To maintain the correct ratio of impeller tip flow area to throat area, A_1 should be replaced by A_{th} and A_2 should be halved in Equation (3.22):

$$A_R = \frac{A_2 \sin \beta_2}{A_1 \sin \beta_{th}}. \quad (3.22)$$

3.8 Summary

The mean-line code, as initially developed for centrifugal impeller design and analysis was adapted, after which different impellers were analysed. The two areas of adaptation were the slip formulation employed in the code, and the location and calculation of the throat area. Three different iterations of the code, *original*, *first*, and *second* were developed and each impeller was analysed using each iteration of the code. The results of the mean-line analyses are discussed in Chapter 5.

Chapter 4

Computational Fluid Dynamics

This chapter is concerned with the 3-D analyses of the impellers under consideration in this study. The process that was followed to set up the 3-D analyses is discussed and mesh details for each impeller is given.

4.1 Introduction

The analysis of an impeller through the use of a mean-line code, followed by a Computational Fluid Dynamics simulation forms part of this project. The mean-line code is used to get a first approximation for the pressure ratio and efficiency of the impeller. A CFD analysis is completed once the mean-line results are known and is then compared to the mean-line results. The k27 impeller was used to complete the benchmark analysis, which is the same impeller that was numerically analysed by Van der Merwe (2012). The k27 impeller was originally designed for a turbocharger in the trucking industry, but turned out to be popular as a performance component in the aftermarket modification of street cars (Van der Merwe, 2012).

This chapter contains details concerning the meshing of the k27, Van der Merwe, and Diener impeller geometries and the set-up of the CFD analyses. Numeca software was chosen to perform the CFD analyses. AutoGrid5™ and FINE™/Turbo are dedicated software for generating meshes and setting up a flow analyses respectively for turbomachinery.

4.2 Impeller Geometry

The impeller geometry is required in order to create a computational mesh for the CFD analysis. Several file formats can be imported into Numeca AutoGrid5™ in

order to create an impeller geometry, such as an IGES file from a Computer Aided Design (CAD) surface model. A simpler method is the use of a geometry file that already describes the defining curves of an impeller geometry. Once the geometry of the impeller is defined, the CFD pre-processor is used to create a mesh for the compressor domain.

4.2.1 Geometry File Format

The geometry file, in *geomTurbo* file format is used as an input for Numeca's AutoGrid5™ where a workable mesh is prepared. A general description of the *geomTurbo* file format is given in Appendix C. The file contains information regarding the hub and shroud contour curves, and blade pressure and suction side curves. These points are either described in a Cartesian or cylindrical coordinate system. When read by Numeca AutoGrid5™ the respective surfaces are created: the hub and shroud surfaces by revolving their defining curves around the z-axis, and the blade surfaces by lofting the pressure and suction curves as shown in Figure 4.1.

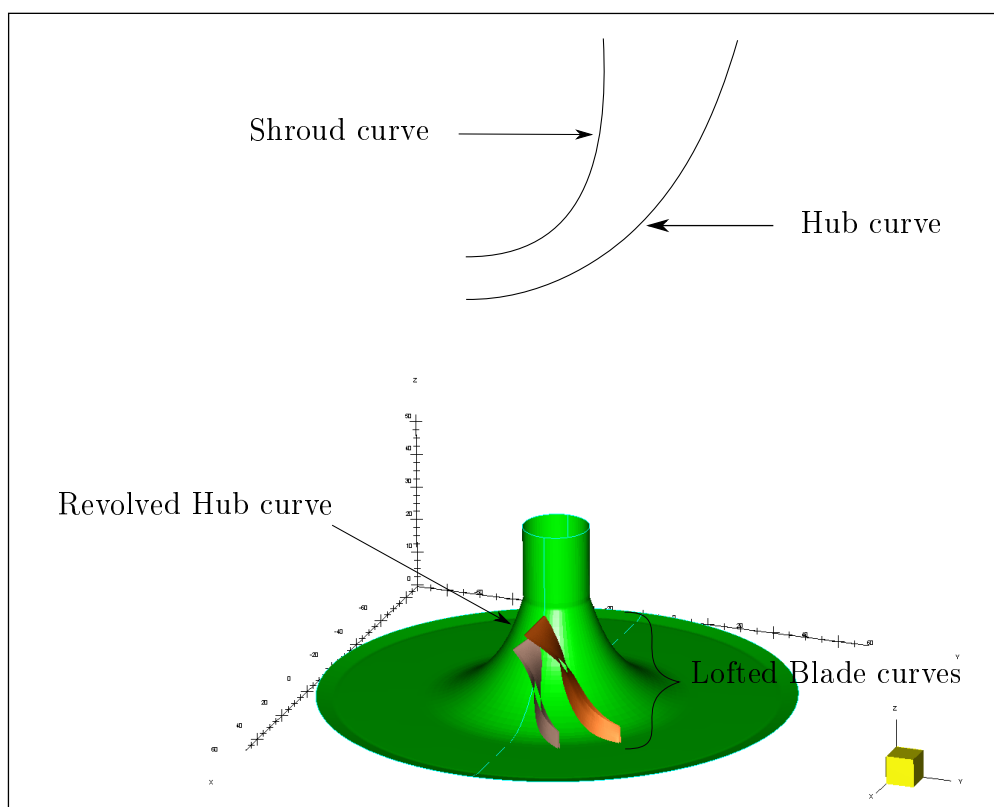


Figure 4.1: Curves and Surfaces Defining k27 Impeller Geometry

A new geometry file can be generated in three different ways:

- Numeca Autoblade™/ Autogrid™ can be used to create a geometry from scratch with sketching tools.
- A custom code with impeller parameters as input that creates the necessary curves based on the input parameters and then writes a geometry file containing the generated curves can be used.
- A custom code and geometric measurements and/or scans can be used to create a surface model and the necessary curves from the surface model can then be imported into either Autoblade™, Autogrid™ or IGG™.

For all three of the k27, Van der Merwe, and Diener rotors the impeller parameters are known. The exact impeller geometry was however required in order to perform a benchmark analysis. It was not necessary to generate a geometry file for the Van der Merwe optimised impeller and Diener impeller as geometry files for these impellers are available. For the k27 impeller, however, a geometry file had to be created as one was not available. An impeller CAD model of the k27 impeller that was created through geometric scans was used to generate the geometry file through importing the impeller curves of the CAD model into Autogrid™. The process of the scans are discussed in Section 4.2.2.

4.2.2 Geometric Scans

Since the k27 impeller is an existing impeller, it was possible to create an accurate CAD surface model through geometric scans of the existing k27 impeller. Van der Merwe (2012) performed geometric scans on the k27 impeller through an optical scanner, creating a point cloud of the geometry. This was done multiple times with different orientations of the impeller in order to scan all the important geometric features of the impeller. The multiple scans were then superimposed using fixed coordinate stickers on the model.

The resulting point cloud was then exported in *stl* format to be processed by CAD software (Van der Merwe, 2012). The author thus used the already existing *stl* file of the k27 impeller created by Van der Merwe (2012) to create a surface model of the geometry using Autodesk® Inventor® Professional 2018. The CAD surface model was exported in *IGES* file format and imported into AutoGrid5™.

4.3 Computational Domain

The computational domain for the benchmark CFD analysis is shown in Figure 4.2. The k27 impeller serves as the benchmark for the CFD analysis. The computational domain stretches from the inlet of the compressor to the outlet of the vaneless diffuser. An extended outlet with a pinch is shown in Figure 4.2. The extended outlet with the pinch is employed to overcome backflow at the outlet boundary. Figure 4.3 shows the computational domain of the mixed-flow impeller of Diener (2016). The position of the blade is shown, together with the starting point of the splitter blade.

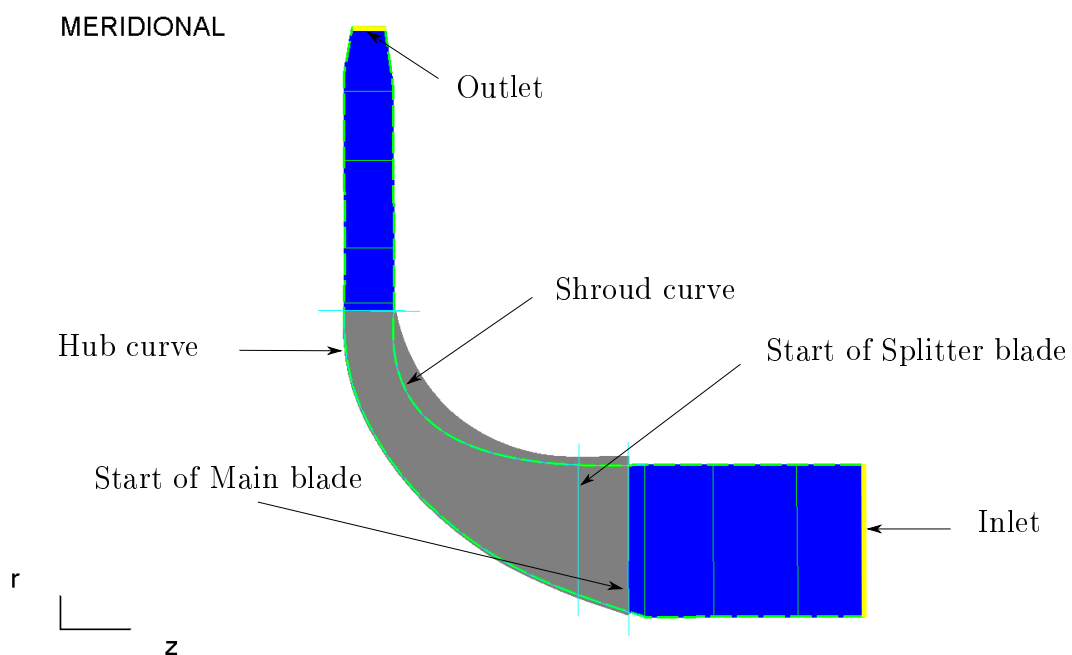


Figure 4.2: k27 Computational Domain

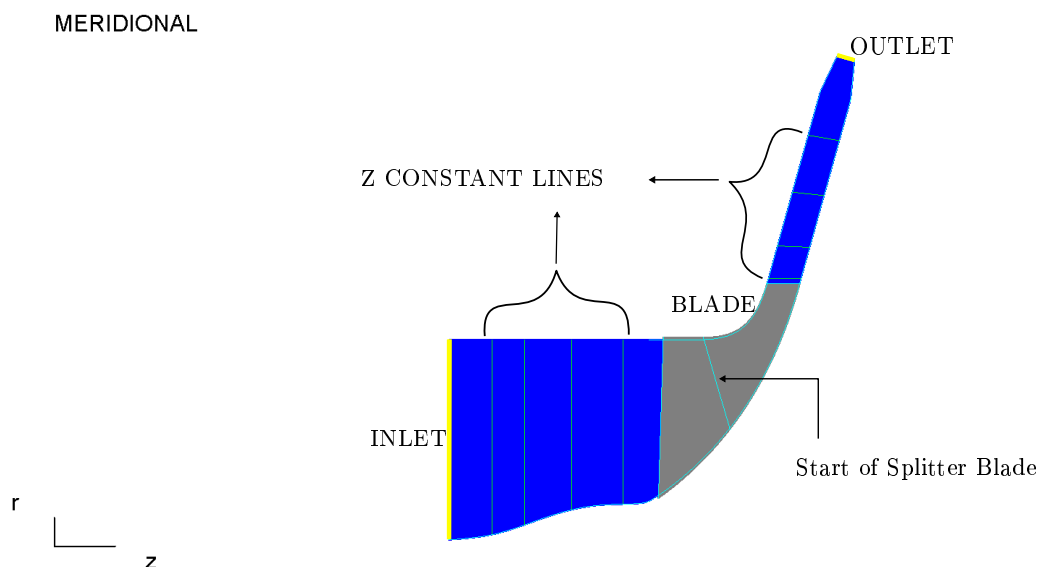


Figure 4.3: Diener Impeller Computational Domain

4.4 Mesh Generation

AutoGrid5TM was used to create a structured mesh within the impeller computational domain. Structured meshes allow the user more control over the mesh and subsequently a higher degree of quality. This in turn leads to better alignment of mesh cells (in the direction of the flow) and better convergence of simulations. The interface allows a geometry file to be imported after which a row wizard is followed to set up an initial mesh. It is however necessary to adjust certain parameters to attain a mesh of good quality.

The k27 and optimised Van der Merwe impeller was modelled using seven periodic volumes and the Diener impeller with nine periodic volumes, each consisting of one main blade and one splitter blade. An impeller rotational speed of 120 krpm was specified for the k27 and Van der Merwe impeller, while a Rotational Speed of 95 krpm was specified for the Diener impeller. Blade fillets were omitted in the modelling of all impellers as they present a significant challenge in obtaining an acceptable mesh quality. Van der Merwe (2012) found that omitting the blade fillets had less than a 3% deviation in the compressor performance and also states that blade fillets were omitted in his analysis.

Clearance gaps of $t = 0.45 \text{ mm}$, $t = 0.27 \text{ mm}$, and $t = 0.2 \text{ mm}$ were assigned to both the leading and trailing edges of the main and splitter blades for the k27,

Van der Merwe, and Diener impellers respectively.

The wall cell width value was specified to facilitate a y_1^+ value between 1 and 10 on the surfaces of the impeller, as recommended for the Spalart-Allmaras turbulence model. A truncated series solution of the *Blasius* equation for turbulent flow was used to calculate the cell width at the wall, y_{wall} (Numeca International, 2018):

$$y_{wall} = 6 \left(\frac{V_{ref}}{v} \right)^{-\frac{7}{8}} \left(\frac{L_{ref}}{2} \right)^{\frac{1}{8}} y_1^+ \quad (4.1)$$

where V_{ref} can be taken as the average inlet velocity, v as the kinematic viscosity and L_{ref} as the reference length. The distance between the hub and shroud curves upstream of the first row of blades was used as the reference length. If the mass flow is known, the reference velocity can be calculated using the density and cross-sectional area of the inlet. Using Equation (4.1) the wall cell width was calculated to be 20 μm . The number of flow paths was set to the default value of 57.

The next step was to specify a target number of grid points. After a target number of grid points has been specified, a preview of the Blade-to-Blade mesh can be viewed. The preview includes an estimation for the minimum skewness angle and the maximum expansion ratio. The properties of the mesh were edited further in order to create a mesh that fulfils the minimum mesh requirements. 120 Iterations was specified for optimising the channel mesh, while 300 steps were specified for the optimisation of the mesh in the gap. The optimisation is an elliptic smoother applied to the mesh to ensure a smoother distribution of mesh cells. In order to force the optimiser to increase the orthogonality of all cells throughout the mesh, as opposed to only cells at the wall, medium skewness control was applied. The optimiser was specified to perform the optimisation of the mesh on 51 layers by defining the span interpolation as 2%. To ensure that the first cell width at the walls meet the turbulence model y^+ requirement, a cell width of 20 μm at the blade wall was enforced. The y^+ values were analysed in the post-processing environment to ensure that an appropriate first cell width was achieved. Where the y^+ values exceed the recommended range, the mesh was updated with a smaller cell width and the simulation was repeated. The y^+ values for the k27 impeller at its design point are shown in Figure 4.4.

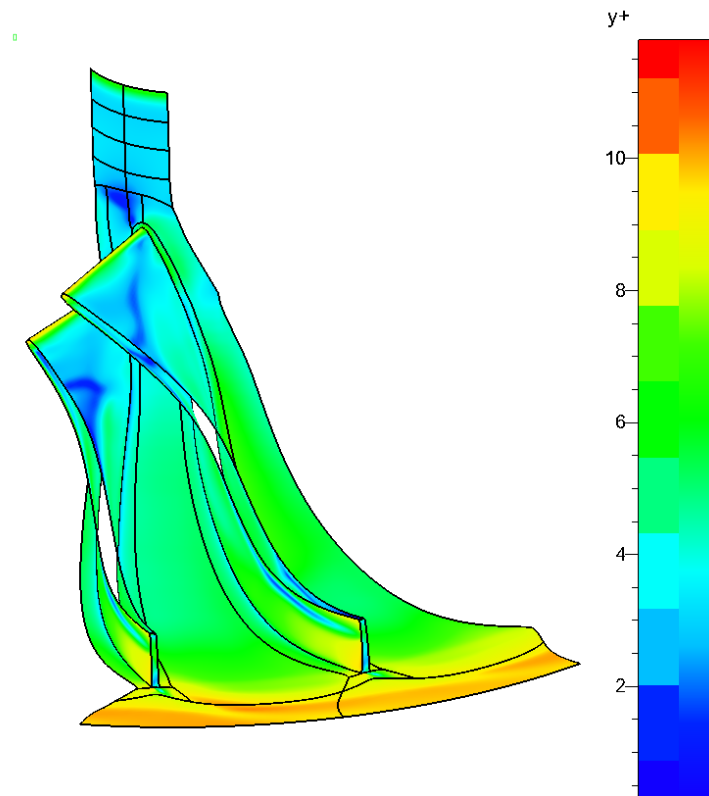


Figure 4.4: y^+ Values of the k27 Impeller at Design Point. $m_{design}=0.277$ kg/s

AutoGrid™ uses the H&I blade topology for meshing centrifugal impellers. Van der Merwe (2012) mentions that the H&I blade topology is typically used when splitter blades are employed. The H&I topology consists of an H-block, a Skin block and an Inlet- and outlet-block. The H-block is used to mesh the blade passage. The grid points for the main and splitter blades for the k27 rotor are shown in Figure 4.5.

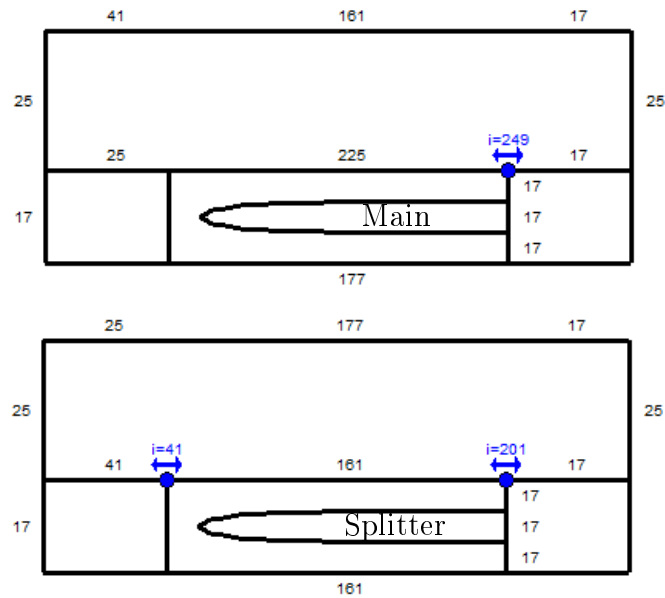


Figure 4.5: k27 Impeller H&I Topology for Main and Splitter Blades

Once the mesh properties have been adjusted and set, the *Topology and Grid Point Distribution* is initialized for the impeller. The flow paths through the computational domain are generated and the Blade-to-Blade mesh can be seen. The final step is to generate the 3-Dimensional mesh. Once the 3-Dimensional mesh has been generated, the mesh quality is evaluated. The quality of the grid is evaluated to ensure solver stability and convergence of the solution. There are four major quality criteria that need to be adhered to, in order to ensure that the mesh is of suitable quality. These criteria are defined as follows:

- Orthogonality is the minimum angle between the edges of a cell (measured in a 2-dimensional plane) and has a value between 0° and 90° .
- Aspect ratio is given as the length of a cell divided by its width, with a value ranging between 1 and 50,000.
- Expansion ratio is the size variation between two adjacent cell surfaces in a specific direction, ranging between 1 and 100.
- Angular deviation is the deviation in angle between two adjacent cell surfaces measured in all directions, with a range between 0° and 180° .

Table 4.1: k27 Mesh Quality

Quantity	Critical Value	Suggested Range	% bad cells
Orthogonality (deg)	23.71	>20	0
Expansion ratio	1.89	<2.5	0
Angular deviation (deg)	8.56	<45	0
Aspect ratio	140.95	<2500	0

Table 4.2: Van der Merwe optimised impeller Mesh Quality

Quantity	Critical Value	Suggested Range	% bad cells
Orthogonality (deg)	17.77	>20	0.0005
Expansion ratio	2.56	<2.5	0.00001
Angular deviation (deg)	57.82	<45	0.00007
Aspect ratio	1045.5	<2500	0

Table 4.3: Diener impeller Mesh Quality

Quantity	Critical Value	Suggested Range	% bad cells
Orthogonality (deg)	10.96	>20	0.0006
Expansion ratio	4.11	<2.5	0.00047
Angular deviation (deg)	27.15	<45	0.00025
Aspect ratio	538.51	<2500	0

Table 4.1, 4.2, and 4.3 show the mesh quality for the k27, optimised Van der Merwe, and Diener impellers respectively, along with the suggested range and the subsequent percentage of bad cells. The critical value refers to the worst value recorded for the mesh. The mesh for the k27 benchmark analysis fulfilled all the requirements of the mesh criteria for all mesh cells. The meshes of the Van der Merwe and Diener impellers did however have mesh cells with critical values exceeding the suggested range, but with a small number of bad cells. A mesh independency study was also conducted to prove that mesh density has no significant effect on the calculated results. The details of the mesh dependency study are given in Appendix E. Figure 4.6 shows the final mesh for the k27 impeller in the $m - \theta$ plane with a periodicity of two and the 3-D mesh with a periodicity of one respectively.

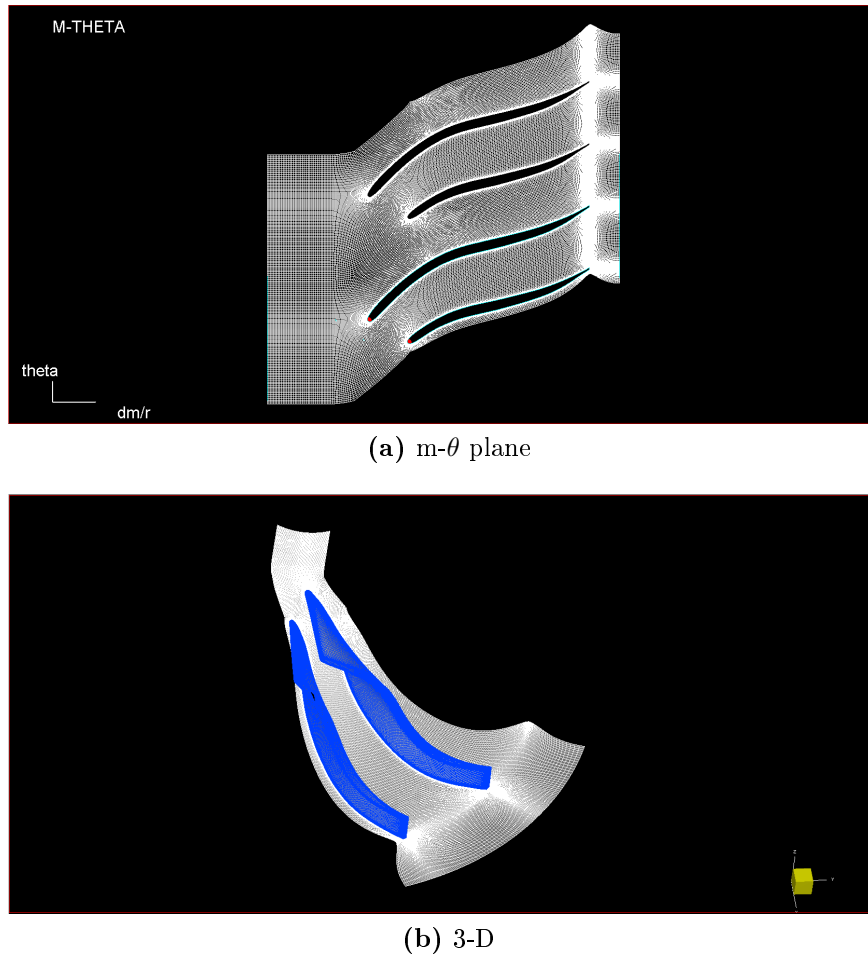


Figure 4.6: Final Mesh for the k27 Impeller

4.5 Fluid and Flow Model

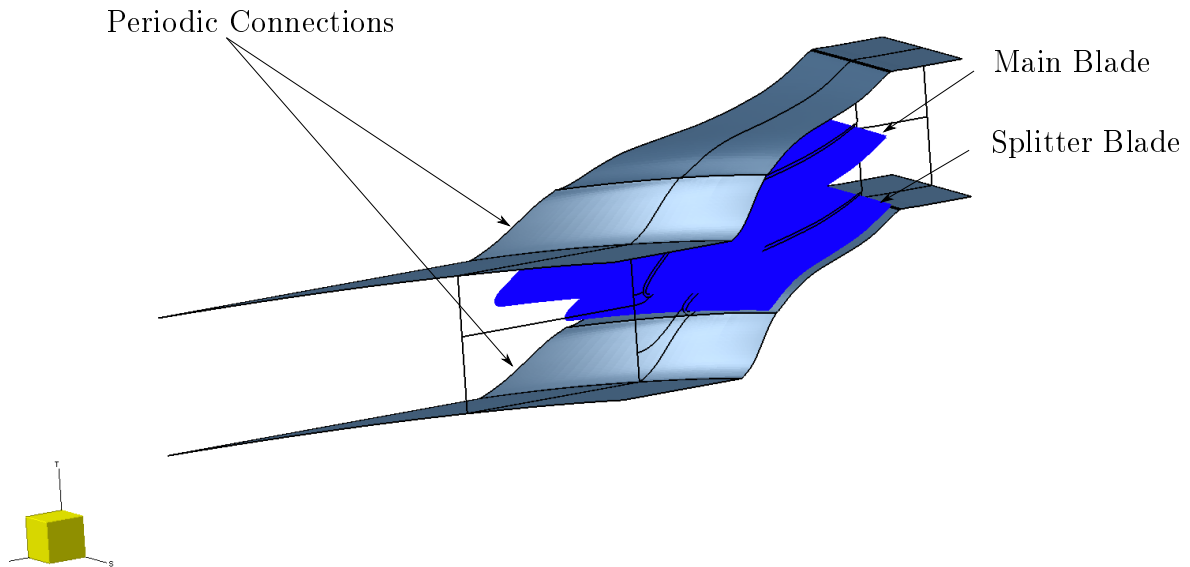
The fluid selected as the operating gas in this study was air. For the simulations in FineTM/Turbo, air as a calorically perfect gas was selected, instead of air as a real gas or incompressible gas. Both Krige (2013) and Le Roux (2010) simulated both the real gas and calorically perfect gas and the two gas models proved to give similar results. For air as a perfect gas the Sutherland law is employed as the viscosity law. The time configuration for this study was steady as steady state compressor operation was assumed. The Reynolds-average Navier-Stokes (RANS) equations were selected to govern the steady-flow physics.

The Spalart-Allmaras model was used as the turbulence model. The Spalart-

Allmaras model is a one-equation model that solves the Reynolds-averaged Navier-Stokes equations and a transport equation for the turbulence model. The Spalart-Allmaras turbulence model has shown to give good performance in boundary layers with adverse pressure gradients, which are important for predicting stalled flows. It has therefore been found to be suitable for aerofoil applications and thus popular for modelling turbomachinery (Spalart and Allmaras, 1992). Van der Merwe (2012) compared simulation results of the Spalart-Allmaras, Baldwin-Lomax, k-epsilon, and k-omega models with the results being within 3% of each other. The Spalart-Allmaras model is favoured above the other models because of its quicker computation time, reduced memory requirements and good accuracy (De Wet, 2011; Van der Merwe, 2012).

4.6 Boundary Conditions

The compressor was modelled using periodic volumes. Figure 4.7 shows the periodic connections in dark grey with the blades coloured in blue. The periodic volume is defined from the pressure side of a splitter blade to following pressure side of the next splitter blade in the *tangential* direction and from inlet to outlet in the *z*-direction.

NUMECA**Figure 4.7:** Periodic Boundary Connections

The boundary conditions are defined in four main boundary groups:

1. Inlet

A cylindrical coordinate system with a subsonic inlet boundary was assigned. The flow was assumed to enter the compressor in an axial direction and should therefore be constrained in the z -axial direction in a cylindrical coordinate system. A velocity extrapolated boundary condition was assigned to constrain the velocity components (V_r, V_t, V_z). Table 4.4 shows the imposed quantities for the inlet boundary.

Table 4.4: Inlet Boundary Imposed Quantities

Property	Value
$V_r/ V $	0
$V_t/ V $	0
$V_z/ V $	1
Absolute Total Pressure	101325 Pa
Absolute Total Temperature	293 K
Turbulent Viscosity	0.0001 m^2/s

2. Outlet

An averaged static pressure boundary condition was imposed for the outlet, since the approximation of a uniform static pressure at the outlet is not accurate. This boundary condition extrapolates a pressure profile from the interior field (Numeca International, 2018). *Backflow Control* was enabled as the outlet was of a radial diffuser type. This option controls the temperature distribution along the exit section. This ensures that in the case of flow partially re-entering, the reverse flow temperature is adjusted to have the same averaged value as that of the exiting flow.

3. Periodic boundaries

One important feature of the AutoGrid5TM mesh generator concerns the automatic establishment of all connecting and periodic boundary conditions. When importing the mesh file created in AutoGrid5TM to FINETM/Turbo, the properties of the periodic boundaries are transferred to the FINETM/Turbo interface, with the advantage that the user does not need to specify any input concerning these boundary conditions.

4. Wall boundaries

The wall boundaries include the impeller hub, shroud and blades. The hub and blade surfaces rotate at the same speed relative to the stationary shroud wall, modelled as rotating walls, while the shroud surface remains static. The rotational speed of the rotating surfaces was set to the same speed as the required impeller speed. Smooth surfaces and no heat transfer (adiabatic flow) was assumed for all wall boundaries. The boundaries were defined in the cylindrical coordinate frame for the rotating blocks and no rotor-stator interface was selected as only the impeller was modelled.

4.7 Settings

NUMECA's solver for FINETM/Turbo, EURANUS, allows for a multigrid strategy to efficiently solve flow equations. This multigrid strategy makes use of coarse grid initialisation, which uses the coarser grid level solutions as an initial solution for the finer grid levels. AutoGrid5TM creates meshes with three grid levels, namely 000, 111 and 222, where 000 is the finest grid level and 222 is the coarsest grid level. It indicates for each of the i , j , and k directions, the currently selected grid level. The current grid level was set to be the finest and the number of grid levels employed for the coarse grid initialisation was 3. Under the Expert Parameters, linear progression was selected as the Scheme definition used for the sweeps on each grid level. By selecting linear progression for the solver, the number of sweeps performed on each grid level equals the level number, e.g. 2 sweeps on

the second level. The spatial discretization was set to central for all grid levels. The maximum number of cycles per grid level varied from 200 to 500 while the convergence criteria for each grid level was set to -4.

The *CFL* (Courant-Friedrich-Levy) number is used to globally scale the time-step size used for the time marching scheme of the flow solver. For faster convergence a higher *CFL* number can be selected, but will lead to divergence if the stability limit is exceeded (Numeca International, 2018). A value of three was used.

Five options exist for specifying the initial solution. The turbomachinery option is dedicated to turbomachinery applications that were meshed by AutoGrid5™. This option respects the inlet and outlet boundary conditions and assumes a constant rothalpy along axisymmetric stream surfaces. The velocity field is also automatically aligned with the blade passage.

Several quantities can be selected to be written to the solution file (*.cgns) from the *Output* window. The pressure, temperature, density, entropy, velocity, Mach number, and wall- y^+ were selected to be recorded.

The Fine™/Turbo GUI allows the user to monitor several residuals as requested by the user. The requirements for convergence is defined by the user in the *Control Variables* window. The convergence criteria was set to be a decrease of 6 orders of magnitude, while a minimum of 1000 iterations were specified. Convergence is said to be satisfactory when the following criteria have been met:

- the global residual has decreased by at least three orders of magnitude,
- the global performance has completely stabilised, and
- the inlet and outlet mass flows have converged to a difference of less than 1%.

Figure 4.8 shows the global convergence and Figure 4.9 shows the mass flow rate convergence. Both convergence graphs shown is for the k27 impeller.

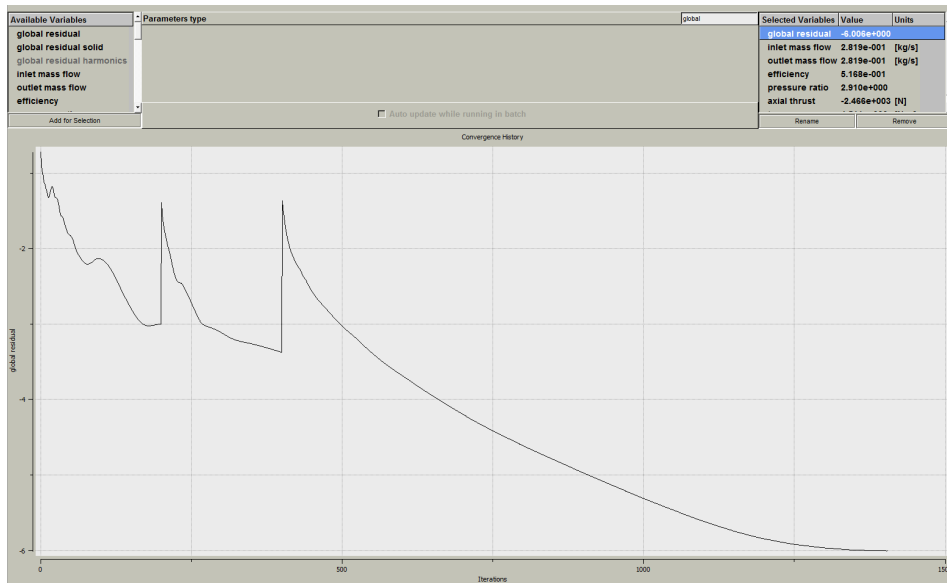


Figure 4.8: Global Convergence History

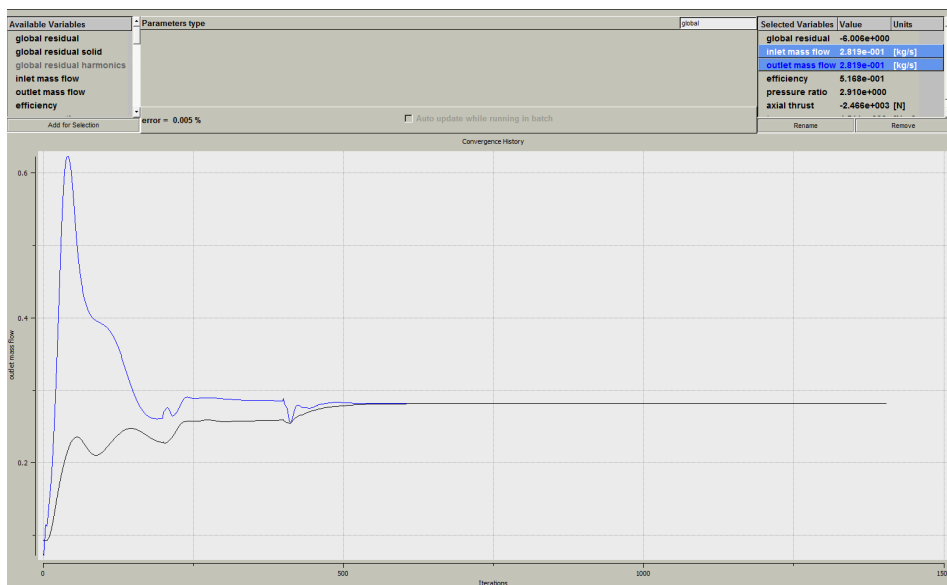


Figure 4.9: Mass Flow Convergence History

4.8 Post-processing

CFView™ is a parallelised scientific visualisation software system that was used for the post-processing. In order to evaluate the performance of the impeller only, a post-processing macro was created that enables the required properties such as total pressure and total temperature to be evaluated at a user-defined constant radius plane. Together with CFView™ the NUMECA result file (*.mf) was used. The relevant performance parameters, as well as the mass flow at inlet and outlet of the flow domain, are listed in the result file.

4.9 Summary

The computational domain and mesh set-up for the k27, optimised Van der Merwe, and Diener impellers are discussed in this chapter. The mesh quality for each impeller is shown, and the flow solver set-up is discussed. The results of the 3-D CFD analyses are presented in Chapter 5.

Chapter 5

Results and Discussion

In the presented study, several numerical simulations, comprising of both 1-D and 3-D analyses, have been performed in order to assess the performance of several compressor impellers. The in-house 1-D Matlab[®] code was also adapted to accommodate mixed-flow impellers. The following section details the results of the investigation.

5.1 Mean-Line Code Results

In adapting the in-house 1-D mean-line code, several iterations of the code was developed. Each iteration represents a different amendment of the code. The *original* designation represents the original code as developed by De Wet in 2011 and adapted by Van der Merwe. The *original* code serves as the baseline for all other iterations. The *first* iteration designation refers to the code implementing the new Ji *et al.* (2010) slip factor formulation as discussed in Section 3.7.1. The *second* iteration represents the adaptation of the throat area prediction of the impeller as discussed in Section 3.7.2, while the new slip factor is also employed.

The *first* and *second* iterations of the mean-line code allows insight into the effect of the slip factor and the throat area on the performance prediction for different configuration rotors. Each impeller was analysed using both iterations of the code as well as the original version of the mean-line code in order to quantify the effect of each adaptation on each rotor.

Table 5.1: Summary of Performance Results for the Different Code Iterations for Different Rotors

Impeller	Design Point	Code Iterations		
		<i>original</i>	<i>1st</i>	<i>2nd</i>
k27	$\Pi_{t-t} = 4.75$ $\eta_{t-t} = 87\%$	$\Pi_{t-t} = 4.24$ $\eta_{t-t} = 85.53\%$	$\Pi_{t-t} = 4.17$ $\eta_{t-t} = 85.53\%$	$\Pi_{t-t} = 3.98$ $\eta_{t-t} = 84.32\%$
Van der Merwe: m-l	$\Pi_{t-t} = 4.14$ $\eta_{t-t} = 89.7\%$	$\Pi_{t-t} = 4.15$ $\eta_{t-t} = 89.49\%$	$\Pi_{t-t} = 4.07$ $\eta_{t-t} = 89.38\%$	$\Pi_{t-t} = 3.58$ $\eta_{t-t} = 87.64\%$
Van der Merwe: optimised	$\Pi_{t-t} = 5.34$ $\eta_{t-t} = 91.6\%$	$\Pi_{t-t} = 4.34$ $\eta_{t-t} = 65.16\%$	$\Pi_{t-t} = 4.33$ $\eta_{t-t} = 65.31\%$	$\Pi_{t-t} = 4.26$ $\eta_{t-t} = 65.43\%$
Diener	$\Pi_{t-t} = 5.25$ $\eta_{t-t} = 86\%$	$\Pi_{t-t} = 5.84$ $\eta_{t-t} = 90.75\%$	$\Pi_{t-t} = 6.05$ $\eta_{t-t} = 90.78\%$	$\Pi_{t-t} = 5.63$ $\eta_{t-t} = 90.18\%$

Table 5.1 summarises the performance results for different impellers as predicted by the various iterations of the Matlab[®] 1-D mean-line code. The design point values for each impeller were obtained from CFD analyses. The first entry in the table shows the performance predictions for the k27 impeller. A decrease in both the pressure ratio and efficiency can be seen for every progression of the code. The second and third entries list the results for the two impellers of Van der Merwe (2012). Van der Merwe used the mean-line code to design a centrifugal compressor impeller to adhere to specific performance and dimensional requirements. The second impeller entry (Van der Merwe: m-l) in Table 5.1 refers to the mean-line design as produced by the 1-D Matlab[®] code and the third entry refers to the final impeller as produced by the optimisation process in CFD. The design was optimised using an Artificial Neural Network (ANN) and Genetic Algorithm.

Comparing the results between the mean-line and optimised impeller for the *original* code shows a large difference in efficiency. This result is not expected, but can be explained by the change in the blade outlet angle between the impellers. The optimised impeller has a blade outlet angle of $\beta_2 = 90^\circ$, compared to $\beta_2 = 60^\circ$ for the mean-line impeller. Analysing the results of the different sections making up the code showed a significant difference in the predicted temperature ratio, leading to the large discrepancy in efficiency (refer to Equation (2.6)). Upon further investigation of the equations which influence the total outlet temperature calculation, a significant difference in the recirculation work input coefficient, I_R , was found.

The change in outlet angle resulted in the recirculation coefficient I_R changing from 0.0244 to 0.287, with the larger outlet angle resulting in more recirculation work. This can be explained by considering the equation for the recirculation coefficient, Equation (5.1):

$$I_R = \left(\frac{D_{eq}}{2} - 1\right) \left[\frac{W_{U2}}{C_{m2}} - 2\cot(\beta_2)\right]. \quad (5.1)$$

The effect of the blade outlet angle on the recirculation coefficient is contained in the last term of Equation (5.1). When the blade outlet angle nears 90° the last term effectively falls away and I_R increases. The blade outlet angle is however not the only value that has a significant impact on the recirculation coefficient, with the relative tangential velocity and absolute meridional velocity also affecting I_R . This is important to note as the efficiency recorded for the Eckardt "O" rotor by De Wet (2011), which also has a blade outlet angle of 90° , as predicted by the original mean-line code correlates well with experimental and CFD results, predicting an efficiency between 80% and 85%. This result is not expected (on the basis of the Van der Merwe optimised rotor results) as the blade outlet angle is also 90° , but the blade tip speed is 1.6 times smaller than that of the optimised Van der Merwe rotor and thus the relative tangential velocity, W_{U2} , is much smaller, leading to a small recirculation coefficient and subsequently to a higher efficiency.

5.2 k27 Impeller

Figure 5.1 shows the results for the k27 impeller, comparing both the 1-D mean-line and CFD results from this study to that obtained by Van der Merwe (2012). There is a discrepancy in the results for the mean-line as well as for the CFD results between this study and that of Van der Merwe. The discrepancy in the CFD results is attributed to both the different computational domains (as the exact computational domain used by Van der Merwe is not available) as well as the location of the evaluation plane. It should also be noted that the step gap modelled by Van der Merwe was not modelled in this study.

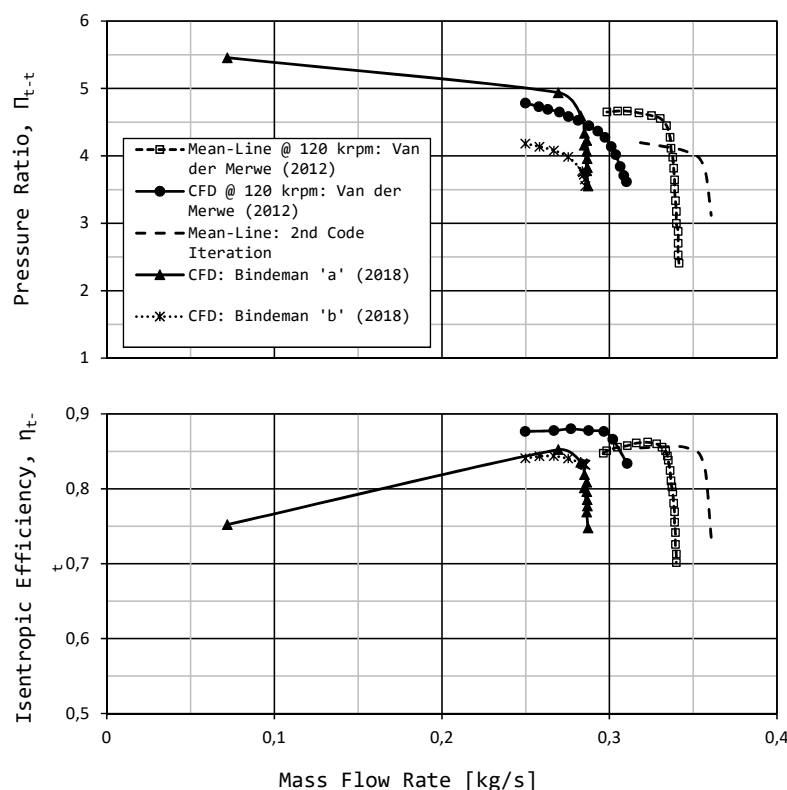


Figure 5.1: Results Comparison for the k27 Rotor at 121 krpm

Figure 5.2 shows two different computational domains for the k27 impeller. The inlet length of the domain in Figure 5.2 (a) is 12.65 mm, with an outlet length of 9.93 mm. For Figure 5.2 (b) the inlet length is 23.72 mm and the outlet length 28.66 mm. The effect of the inlet and outlet dimensions of the two different computational domains is shown in the results presented in Figure 5.1. The exact location where Van der Merwe evaluated the compressor thermodynamic properties is also not known, as only "impeller outlet" was specified by Van der Merwe. A difference of 0.2163 for pressure ratio and 3.52% (absolute) for efficiency is recorded when moving the evaluation plane downstream with 1 mm (from $r = 41$ mm to $r = 42$ mm). The results presented in Figure 5.1 were recorded at $r = 42$ mm. Van der Merwe's (2012) CFD results predict both a higher pressure ratio and efficiency compared to the benchmark (Bindeman 'b' (2018)) CFD results of this study. A 0.6 difference in pressure ratio is recorded, while the efficiencies only differed by 3.6% (absolute) at a mass flow of 0.25 kg/s. A smaller operating range was also

predicted to that of Van der Merwe.

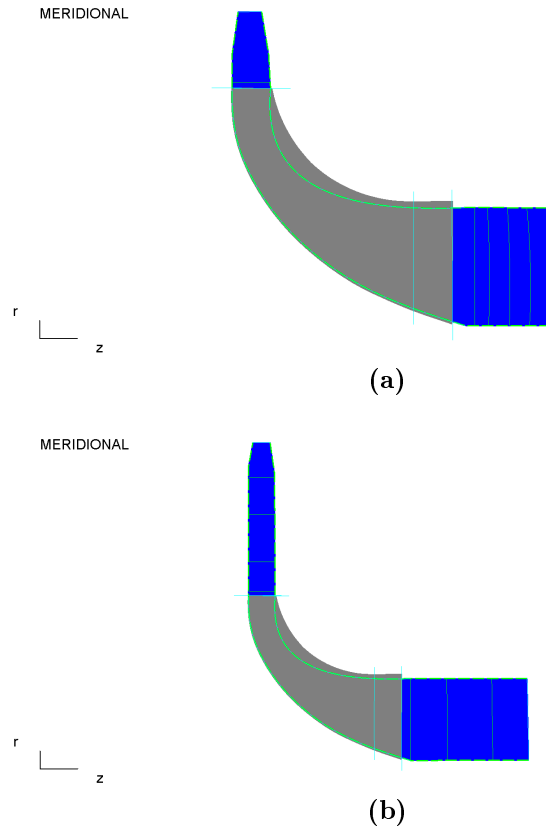


Figure 5.2: Different Computational Domains for the k27 Impeller

The 1-D mean-line results compare relatively well. There is a 0.57 difference in the pressure ratio, but only a 0.019% difference in efficiency between the mean-line codes at the best performing point. It is however interesting to note that the mean-line result of Van der Merwe predicts the onset of choke at a lower mass flow compared to the *second* iteration code. A large discrepancy exists between the four results for the prediction of choke. It is this discrepancy, together with the shock waves present at design speed (121 krpm) shown in Figure 5.3, that prompted the investigation into the location of the throat area and the second iteration of the mean-line code.

NUMECA

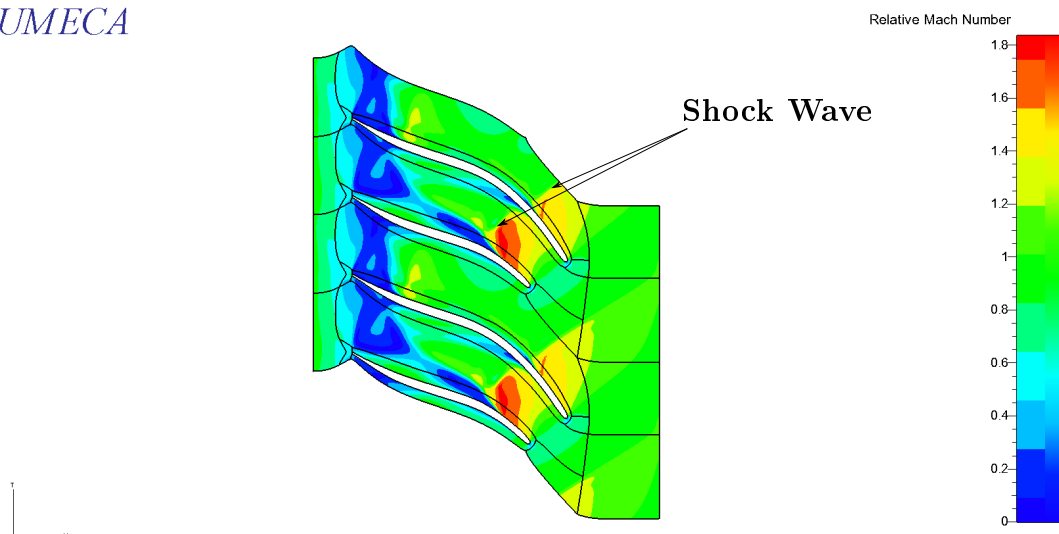


Figure 5.3: Relative Mach Number at 90% Span for the k27 Impeller

5.3 Van der Merwe Impeller

Figure 5.4 shows the performance curves for the mean-line Van der Merwe rotor, comparing the different iterations of the code. The *original* and the *first* iteration of the code show similar performance results, with near identical efficiencies and very similar pressure ratios. The *original* iteration's pressure ratio is 0.7 higher than that of the *first* iteration, while the efficiency of the first iteration is only 0.1% lower than the *original* iteration's efficiency at design point. The *first* iteration of the code also displays the same choke margin for the impeller, whereas choke occurs at a lower mass flow for the *second* iteration (at 0.98 of the design mass flow rate), as expected, since the throat area is smaller than that for the first two iterations of the code. The *second* iteration of the code, for which the throat is located between the main blade and splitter blade, has both a lower pressure ratio and lower efficiency at design point. The *second* iteration's pressure ratio and efficiency are 0.56 and 2.06% lower respectively, compared to the design point conditions for the impeller. A smaller stall region is also predicted for the *second* iteration of the code.

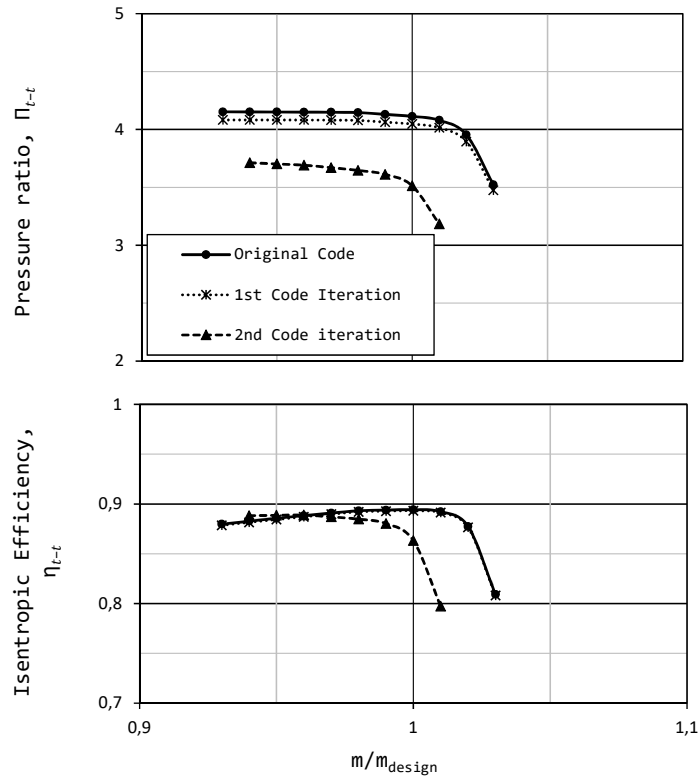


Figure 5.4: 1-D Mean-line comparison of Van der Merwe mean-line rotor at 121 krpm. $m_{design} = 0.325$ kg/s

Figure 5.5 shows a comparison of the performance curves for the Van der Merwe optimised rotor at 121 krpm. The first two iterations of the code for the optimised rotor only differs with 0.1 (absolute) for both pressure ratio and efficiency. Both the choke and stall prediction for the first two iterations of the code is identical. The second iteration of the code predicts a lower pressure ratio, but a higher efficiency. The pressure ratio prediction for the second iteration is 0.15 lower compared to the first two iterations, while the efficiency differs by 1%. The onset of choke takes place at a lower mass flow for the second iteration compared to the first iteration and original version of the code, while the stall region remains the same for all three versions of the code.

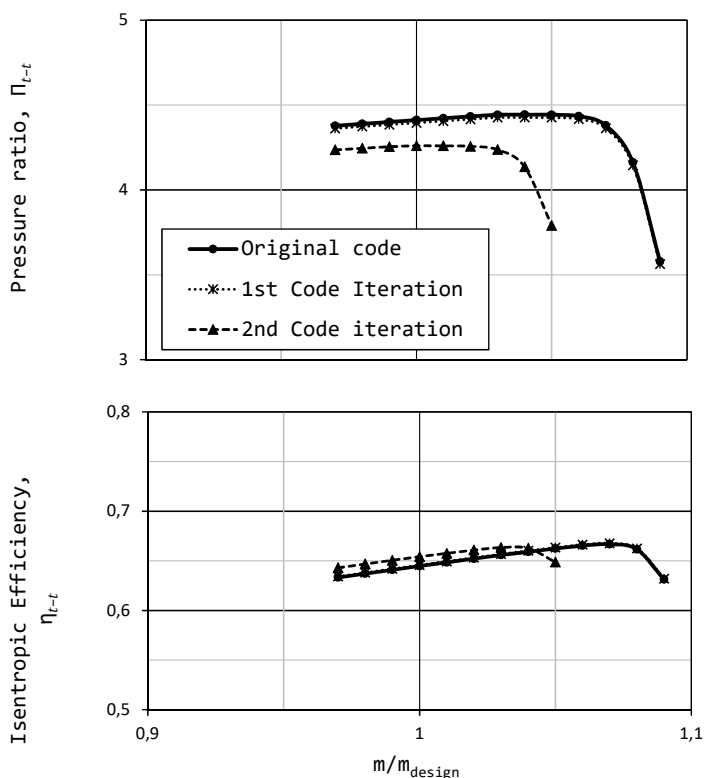


Figure 5.5: 1-D Mean-line comparison of Van der Merwe optimised rotor at 121 krpm. $m_{design} = 0.325$ kg/s

Figure 5.6 shows a comparison of the results for the optimised Van der Merwe impeller. There is an excellent correlation between the CFD results of this study and that of Van der Merwe, but a large difference when comparing to that of the 1-D mean-line prediction. Table 5.1 shows that the mean-line code predicts a lower pressure ratio and efficiency for the optimised Van der Merwe impeller for all three iterations of the code. The pressure ratio at design mass flow rate predicted by the CFD is 5.34, while the mean-line code only predicts a pressure ratio between 4.26 and 4.34 for the three iterations of the code. The mean-line code also under-predicts the isentropic efficiency by 26.3% (absolute). The discrepancy in efficiency is discussed in the beginning of this chapter, while the discrepancy in pressure ratio can be attributed to conservative predictions for the mixing loss and supercritical Mach number loss coefficient. Both of these loss coefficients are indirectly influenced by the blade work input coefficient given by Equation (5.2):

$$I_B = \sigma(1 - \lambda\phi_2 \cot\beta_2) - U_1 C_{U1} / U_2^2. \quad (5.2)$$

The blade work input coefficient affects the average blade velocity difference, ΔW , which then affects the maximum relative velocity, W_{max} . Subsequently, the supercritical Mach number loss coefficient, $\bar{\omega}_{cr}$, is influenced. Similarly to the supercritical Mach number loss, the wake mixing loss coefficient, $\bar{\omega}_{mix}$, is affected by the maximum relative velocity which then affects the equivalent diffusion factor, D_{eq} , which has an influence on determining the separation velocity that is used in the calculation of the wake mixing loss coefficient. The loss models indirectly influence the efficiency as they are only used in the prediction of the outlet pressure.

Similar to Equation (5.1), Equation (5.2) is also influenced by the blade outlet angle, β_2 . When the blade has a pure radial outlet (no back-sweep) it has an adverse affect on the blade work input coefficient and subsequently leads to a too conservative prediction for both the mixing loss and supercritical Mach number loss coefficients. The greater these coefficients, the smaller the predicted outlet pressure. Apart from the discrepancy in pressure ratio and efficiency, a smaller operating range is predicted according to the 1-D mean-line analysis, versus the CFD analysis.

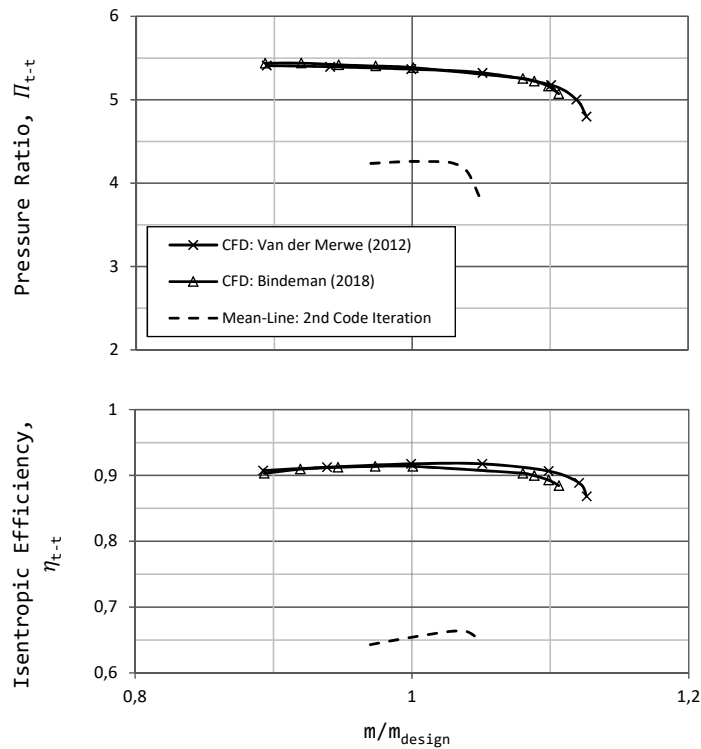


Figure 5.6: Results Comparison for the Optimised Van der Merwe Impeller at 121 krpm. $m_{design} = 0.325$ kg/s

5.4 Diener Impeller

Figure 5.7 shows a comparison of results for the optimised Diener impeller. A discrepancy exists between the CFD results of this study and that of Diener (2016). The difference in the results is due to different inlet conditions used in the set up of the 3-D simulation in FINE™/Turbo. Diener (2016) used 300 K and 100 kPa as the inlet temperature and -pressure respectively. For this study, 293 K and 101325 Pa was used for the inlet temperature and -pressure respectively. A simulation at the impeller's design point with the same inlet conditions used by Diener (2016) was completed to ensure that the discrepancy in results is indeed caused by the difference in inlet conditions. The same inlet conditions used for the set up of the 3-D analysis for this study was used in the mean-line analysis.

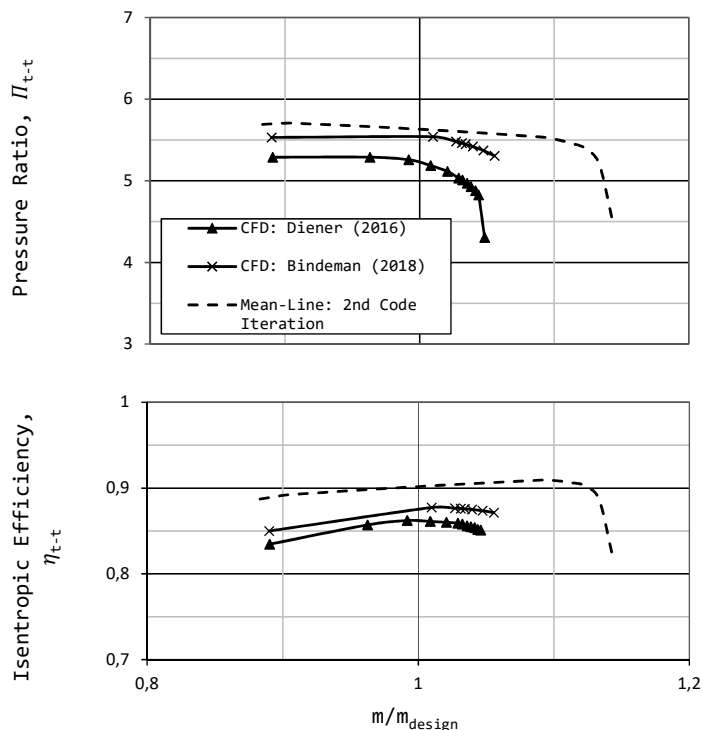


Figure 5.7: Results Comparison for the Final Diener Impeller at 95 krpm.
 $m_{design} = 0.85 \text{ kg/s}$

Although different inlet conditions to that of Diener was used, the curves for both pressure ratio and efficiency have the same shape as that of Diener. Despite a marginal increase being recorded in both pressure ratio and efficiency for the *second* iteration of the mean-line code, it correlates fairly well with the CFD result of this study. There is a 0.1 difference in pressure ratio and a 2.31% in efficiency at the design mass flow rate, when comparing the mean-line prediction to that of the CFD results of this study. Considering Figure 5.7 the correlation between the mean-line code and CFD is quite good. Figure 5.8 shows the relative Mach number plot at 90% blade span for the Diener impeller, taken at the design point. A shock wave upstream of the splitter blade is present as indicated. A smaller shock, compared to the shock upstream of the splitter blade, is also present upstream of the main blade. The largest part of the flow through the impeller can be seen to be near Mach 1 or greater than Mach 1. Considering the state of the flow in compressor impellers, especially the presence of shock waves as in Figure 5.8, an accurate prediction of

performance by a 1-D mean-line code becomes limited. This limitation is due to the inability of a 1-D mean-line code to capture the entire flow field (3-dimensional flow) within an impeller and take all flow phenomenon, such as shock waves, into account when predicting the performance of an impeller. The mean-line code does, however, show the same trend for the pressure ratio and efficiency as that of the two CFD results. Interesting to note is the choke prediction for the mixed-flow impeller by the *second* iteration of the mean-line code. The onset of choke predicted by the *second* iteration is expected to take place at a lower mass flow rate, rather than a higher mass flow rate, when comparing to the CFD, as the throat area was adapted. When considering Figure 5.6 the *second* iteration of the mean-line code can be seen to predict a smaller choke region as expected.

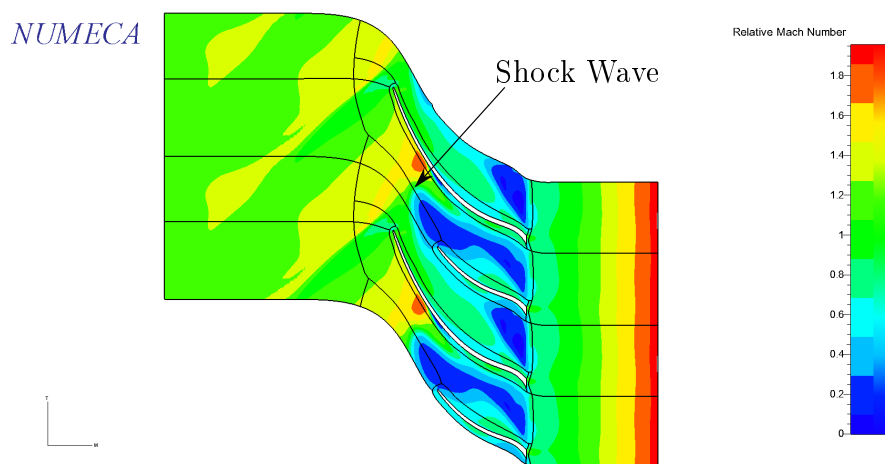


Figure 5.8: Relative Mach Number at 90% Span for the Optimised Diener Impeller

5.5 Summary

The summary of the mean-line code results for each impeller presented in Table 5.1 proved to be valuable in showing the effect of the adaptations made to the code. From this results summary it can be deduced that the throat area, and subsequently the passage area ratio, has a significant influence on the performance prediction of an impeller. The slip factor was also found to have an influence on the mean-line code performance prediction. CFD analyses were completed and serves as a benchmark to compare to the 1-D mean-line results. The discrepancies found between the mean-line results and that of the benchmark CFD analyses proves that the mean-line can only serve as an approximation and a first step in the performance analysis of a compressor impeller.

Chapter 6

Conclusions and Recommendations

The possible applications where MGTs can be used are numerous, while there is an increased interest in the application of MGTs for the propulsion of UAVs. This interest makes the development of a mixed-flow impeller for a specific size-range engine feasible. The use of both 1-D mean-line and 3-D CFD analysis is of importance for a detailed aerodynamic design and performance analysis of such an impeller. Relevant theory concerning mixed-flow impellers and how they function was explained. Literature concerning compressors as well as the 1-D and 3-D analysis of several impellers were detailed.

6.1 Conclusions

Three different compressor impellers were analysed using a 1-D mean-line code developed by De Wet (2011) which is based on the work of Aungier (2000). Two centrifugal impellers, the k27 and Van der Merwe impeller, and the mixed-flow impeller of Diener (2016) were analysed and compared to the results of 3-D CFD analyses. The objective of the thesis was to successfully adapt the in-house mean-line code for application with both centrifugal and mixed-flow impellers. Two specific areas in the code were identified to be adapted; the slip formulation and the throat area. The Wiesner (1967) slip formulation, employed by the original code was replaced with the Ji *et al.* (2010) slip formulation in order to account for the axial flow component in a mixed-flow impeller. An alternative location for the throat area was proposed, calculating the area between a main blade and splitter blade, instead of the area near the inducer section. The results of the adaptations made to the code are presented in Table 5.1, comparing three iterations of the code for each impeller.

The second iteration of the mean-line code under-predicts both pressure ratio and

efficiency for the centrifugal configurations, while it over-predicts efficiency for the mixed-flow configuration (all quantities taken as total-to-total as only the impeller is considered). The pressure ratio is under-predicted by 16.2% and the isentropic efficiency by 3.1% for the k27 impeller. For the mean-line impeller of Van der Merwe the pressure ratio differs by 13.5% and the isentropic efficiency by 2.3%. The optimised Van der Merwe impeller sees the largest difference in the prediction of performance by the mean-line code with a 20.2% and 28.6% deficit in pressure ratio and isentropic efficiency respectively. The performance of the mixed-flow impeller of Diener is, however, predicted more accurately, with a 7.2% and 4.9% over-prediction in pressure ratio and isentropic efficiency respectively by the mean-line code.

At the maximum efficiency point (MEP) of the CFD results for the k27 impeller, there is a 6.15% and 2.95% difference in pressure ratio and isentropic efficiency respectively between the CFD results of this study and that of Van der Merwe (2012). A higher pressure ratio, but lower efficiency is predicted compared to the results of Van der Merwe (2012). The discrepancy in results is due to a different computational domain used. For the optimised impeller of Van der Merwe there is excellent agreement between the CFD results. There is only a 0.35% and 0.41% difference in pressure ratio and efficiency respectively, while Van der Merwe's maximum choke mass flow rate is 1.79% larger.

The mean-line prediction for pressure ratio for the Diener impeller is close to that of the CFD, with a 1.6% increase for pressure ratio and a 2.8% increase for the efficiency. The mean-line code therefore correlates well with the 3-D analysis. It should be noted however that the stall criterion employed in the 1-D analysis had to be changed from 1.75 to 2.5 (user-defined) in order for the compressor curve to be plotted at the design speed of 95 krpm.

It is therefore concluded that the objective of adapting the in-house 1-D mean-line code in order to analyse both centrifugal and mixed-flow impellers was successful. The results of the mean-line analysis for both centrifugal and mixed-flow impellers were compared to 3-D CFD analysis results. It was found that a blade with a pure radial outlet angle ($\beta_{2b} = 90^\circ$) has an adverse effect on the prediction of the 1-D mean-line performance of such an impeller. Furthermore, the throat area was found to have a significant impact on the 1-D mean-line performance prediction. The discrepancies recorded between mean-line and CFD results suggest that a 1-D mean-line analysis is only good enough to serve as an approximation of the expected performance and that a 3-D CFD analysis is still required for an accurate prediction of the performance of an impeller.

6.2 Recommendations

Future work can be done on the adaptation of the 1-D mean-line code. The Ji *et al.* (2010) slip factor chosen in this thesis is only one of many slip factor formulations to choose from. A recommendation is to test more slip factors developed for both mixed-flow and centrifugal impellers or only for mixed-flow impellers and determine if there is one that proves to give reliable results when compared to a benchmark analysis.

The importance of using an accurate throat area for performance prediction is evident and therefore further investigation into the prediction of the throat area and corresponding throat parameters is advised. Both the location and the calculation of the area for the throat can be revised and refined. Critical ratio's, such as the passage area ratio ($\frac{A_2 \sin \beta_2}{A_{th} \sin \beta_{th}}$) and relative velocity ratio ($\frac{W_{th_{shroud}}}{W_{th}}$), that has an influence on both pressure ratio and choke margin are affected by the calculation of the throat area and its location. Special attention should therefore be given to the improvement of all throat parameters. Furthermore, the large discrepancy in performance results for the optimised Van der Merwe impeller suggest that there is merit in investigating the loss models (wake mixing loss and supercritical Mach number loss) and work input coefficients (I_B and I_R) proposed by Aungier (2000). Aungier himself states the "quality of results obtained directly depends on the validity of the empirical models employed" and mentions that the success of a basic analysis system depends on continual validation.

It is also recommended to compare the current in-house mean-line code to commercial software, such as Concepts NREC. Comparing the mean-line code to commercial software will give a better indication of the accuracy of the code. Lastly, the analysis of several mixed-flow geometries available in literature and the documentation of the performance results of each geometry would be of great value to determine the robustness of the code in predicting the performance of a mixed-flow impeller.

List of References

- Aungier, R. (2000). *Centrifugal Compressors*. ASME Press, New York.
- Boyce, M. (1993). Principles of operation and performance estimation of centrifugal compressors. *Proceedings of Turbomachinery Symposium*, vol. 22.
- Boyce, M.P. (2012). *Compressor and Turbine Performance Characteristics*. 4th edn. Elsevier Inc., Oxford. ISBN 9780123838421.
- Burger, C.J. (2016). *Design Procedure of a Compact Aerodynamic Crossover Diffuser for Micro Gas Turbine Application*. Masters, University of Stellenbosch.
- Busemann, A. (1928). Das Förderhöhenverhältnis radialer Kreiselpumpen mit logarithmisch-spiraligen Schaufeln. *ZAMM - Zeitschrift für Angewandte Mathematik und Mechanik*, vol. 8, no. 5, pp. 372–384. ISSN 00442267.
- Cevik, M. (2009). *Design And Optimization Of A Mixed Flow Compressor Impeller Using Robust Design Methods*. Masters, Middle East Technical University.
- Cumpsty, N.A. (1989). *Compressor Aerodynamics*. Longman Scientific & Technical. ISBN 9780582013643.
- De Villiers, L. (2014). *Design of a Centrifugal Compressor for Application in Micro Gas Turbines*. Masters, Stellenbosch.
- De Wet, A.L. (2011). *Performance Investigation of a Turbocharger Compressor*. Masters, Stellenbosch University.
- Diener, O. (2016). *Development of a Mixed-Flow Compressor Impeller for Micro Gas Turbine Application*. Masters, Stellenbosch University.
- Dixon, S. and Hall, C. (2010). *Fluid Mechanics and Thermodynamics of Turbomachinery*. 6th edn. Elsevier Inc., Oxford.
- Dixon, S.L. (1998). *Fluid Mechanics , Thermodynamics of Turbomachinery*. Fourth edn. Butterworth-Heinemann, Oxford.
- Eck, B.F. (1973). *Fans: design and operation of centrifugal, axial- flow, and cross-flow fans*. Oxford University Press, NewYork.

- Eisenlohr, G. and Benfer, F.W. (1994). Aerodynamic Design and Investigation of a Mixed Flow Compressor Stage. *October*, vol. 537, no. October 1993, pp. 20.1 – 20.7.
- Harris, M., Jones, A. and Alexander, E. (2003). Miniature Turbojet Development at Hamilton Sundstrand: The TJ-50, TJ-120 and TJ-30 Turbojets. In: *2nd AIAA "Unmanned Unlimited" Conf. and Workshop & Exhibit*, Infotech@Aerospace Conferences. American Institute of Aeronautics and Astronautics.
Available at: <https://doi.org/10.2514/6.2003-6568>
- Hill, P.G. and Peterson, C.R. (1992). *MECHANICS AND THERMODYNAMICS*. 2nd edn. Pearson.
- Japikse, D. (1996). *Centrifugal compressor design and performance*. Concepts ETI, Wilder, Vt. ISBN 0933283032.
- Ji, C., Zou, J., Ruan, X.D., Dario, P. and Fu, X. (2010). A new correlation for slip factor in radial and mixed-flow impellers. *Power and Energy*, vol. 225, pp. 114–119.
- King, J.A. and Glodeck, E. (1942). Performance Characteristics of Mixed flow impeller and vaned diffuser with several modifications. Tech. Rep., National Advisory Committee for Aeronautics, Cleveland, Ohio.
- Kock, M.P. (2017). *Design of a Cross-over Diffuser for a Mixed Flow Compressor Impeller*. Masters, Stellenbosch.
- Krige, D.S. (2013). *Performance Evaluation of a Micro Gas Turbine Centrifugal Compressor Diffuser*. Masters, Stellenbosch.
- Lakshminarayana, B. (1996). *Fluid Dynamics and Heat Transfer of Turbomachinery*. John Wiley & Sons, New York, N.Y.
- Le Roux, F.N. (2010). *The CFD simulation of an axial ow fan*. Masters, Stellenbosch University.
- Marcellan, A. (2015). *An exploration into the potential of microturbine based propulsion systems for civil Unmanned Aerial Vehicles*. Masters, Delf University of Technology.
- Mirsky, S., Jacobson, W., Tiscornia, D., McWhirter, J. and Zaghoul, M. (2013). DEVELOPMENT AND DESIGN OF ANTISURGE AND PERFORMANCE CONTROL SYSTEMS.
- Monig, R., Broichhausen, K. and Gallus, H. (1987). Application of Highly Loaded Single-Stage Mixed-Flow Compressors in Small Jet-Engines. In: *AGARD Conference Proceedings No.421 Advanced Technology for Aero Gas Turbine Components*.
- Mönig, R., Elmendorf, W. and Callus, H.E. (1993). Design and Rotor Performance of a Compressor. *Journal of Turbomachinery*, vol. 1, no. July 1993.

- Musgrave, D.S. and Plehn, N.J. (1987). Mixed-Flow Compressor Stage Design and Test Results With a Pressure Ratio of 3 : 1. *Journal of Turbomachinery*, vol. 109, no. October 1987, pp. 513–519. ISSN 15288900.
- Numeca International (2018). Fine/Turbo 11.2 User Manual.
- Paeng, K.S. and Chung, M.K. (2001). A new slip factor for centrifugal impellers. *Proceedings of the Institution of Mechanical Engineers, Part A: Journal of Power and Energy*, vol. 215, no. 5, pp. 645–649. ISSN 09576509.
- Pampreen, R.C. and Musgrave, D.S. (1978). A Method of Calculating the Slip Factor of Centrifugal Compressors From Deviation Angle. *Journal of Engineering for Power*, vol. 100, no. 1, pp. 121–128. ISSN 0742-4795.
- Pfleiderer, C. (1961). *Die Kreiselpumpen für Flüssigkeiten und Gase*. 5th edn. Springer, Berlin.
- Qiu, X., Japikse, D., Zhao, J. and Anderson, M.R. (2011). Analysis and Validation of a Unified Slip Factor Model for Impellers at Design and. *Journal of Turbomachinery*, vol. 133, no. October, pp. 1–9.
- Rajakumar, D.R., Ramamurthy, S. and Govardhan, M. (2015). Experimental investigations on effects of tip clearance in mixed-flow compressor performance. *Proceedings of the Institution of Mechanical Engineers, Part G: Journal of Aerospace Engineering*, vol. 229, no. 5, pp. 933–946. ISSN 20413025.
- Sandberg, M.R. (2016). Centrifugal Compressor Configuration, Selection and Arrangement: A User's Perspective. *Proceedings of the Forty-Fifth Turbomachinery Symposium*.
- Saravanamuttoo, H.I.H., Rogers, G.F.C. and Cohen, H. (2001). *Gas Turbine Theory*. 50 years. Prentice Hall. ISBN 9780130158475.
- Shukla, T. (2013). Micro Gas Turbine-A Review. *International Journal on Theoretical and Applied Research in Mechanical Engineering*, vol. 2, no. 3, pp. 2319–3182.
- Spalart, P. and Allmaras, S. (1992). A one-equation turbulence model for recirculating flows. *AIAA Paper 92-0439*. ISSN 16747348. [arXiv:1011.1669v3](https://arxiv.org/abs/1011.1669v3).
- Stanitz, J.D. (1952). Some Theoretical Aerodynamic Investigations of Impellers in Radial- and Mixed-Flow Impellers. *Trans. ASME*, vol. 74, pp. 473–476.
- Stodola, A. (1945). *Steam and gas turbines : with a supplement on the prospects of the thermal prime mover...* New York, N.Y. : Smith, New York, N.Y.
- Van der Merwe, B.B. (2012). *Design of a Centrifugal Compressor Impeller for Micro Gas Turbine Application*. Masters, Stellenbosch.

- Verstraete, T., Alsalihi, Z. and Van den Braembussche, R.A. (2010). Multidisciplinary Optimization of a Radial Compressor for Microgas Turbine Applications. *Journal of Turbomachinery*, vol. 132, no. 3, p. 031004. ISSN 0889504X.
- Vick, M.J., Heyes, A. and Pullen, K. (2010). Design Overview of a Three Kilowatt Recuperated Ceramic Turboshift Engine. *Journal of Engineering for Gas Turbines & Power*, vol. 132, no. September 2010, pp. 092301.1–092301.9. ISSN 07424795.
- Visser, F.C., Brouwers, J.J. and Badie, R. (1994). Theoretical analysis of inertially irrotational and solenoidal flow in two-dimensional radial-flow pump and turbine impellers with equiangular blades. *Journal of Fluid Mechanics*, vol. 269, no. June 1994, pp. 107–141. ISSN 14697645.
- Von Backström, T.W. (2006). A Unified Correlation for Slip Factor in Centrifugal Impellers. *Journal of Turbomachinery*, vol. 128, no. January 2006.
- Wehrly, D. (2014). WREN MW54 Gas Turbine Jet Engine.
- Whitfield, A. and Roberts, D.V. (1981). The Effect of Impeller Tip Design on the Performance of a Mixed Flow Turbocharger Compressor. In: *ASME Gas Turbine Conference and Products Show*, vol. 1, pp. 4–10. Houston, Texas. ISBN 9780791879610. ISSN 04021215.
- Wiesner, F.J. (1967). A Review of Slip Factors for Centrifugal Impellers. *Journal of Engineering for Power*, vol. 89, no. 4, pp. 558–566. ISSN 0742-4795.
- Wislicenus, G.F. (1965). *Fluid Mechanics of Turbomachinery*. 2nd edn. Constable and Company, New York.
- Youssef, N. and Weir, G. (2002). Mixed Flow and Centrifugal Compressor for Gas Turbine Engine.
- Zemp, A., Kammerer, A. and Abhari, R.S. (2010). Unsteady Computational Fluid Dynamics Investigation on Inlet Distortion in a Centrifugal Compressor. *Journal of Turbomachinery*, vol. 132, no. 3, p. 031015. ISSN 0889504X.

Appendix A: Impeller Geometry Parameters

The main parameters defining the impeller geometry for each impeller analysed by the mean-line code is given in the following tables. All angles are with respect to the tangential direction. The main parameters for the k27 impeller is shown in Table A.1.

Table A.1: Main Geometrical Parameters for the k27 Impeller

Parameter	Value
Blade number	7
r_1_hub	10.113 [mm]
r_1_shroud	25.522 [mm]
r_2_shroud	40.439 [mm]
Impeller height	28.814 [mm]
β_{1_hub}	58 [deg]
β_{1_shroud}	30 [deg]
β_2	57 [deg]
LE_hub	1.52 [mm]
LE_shroud	0.817 [mm]
TE	0.488 [mm]
b_2	4 [mm]
CL	0.45 [mm]
α_{c2}	90 [deg]

The main parameters for the mean-line Van der Merwe impeller is shown in Table A.2.

Table A.2: Main Geometrical Parameters for the Van der Merwe m-l Impeller

Parameter	Value
Blade number	7
r_1_hub	8.138 [mm]
r_1_shroud	26.01 [mm]
r_2_shroud	37.5 [mm]
Impeller height	30 [mm]
β_{1_hub}	52 [deg]
β_{1_shroud}	24.6 [deg]
β_{2}	60 [deg]
LE_hub	2 [mm]
LE_shroud	0.6 [mm]
TE	0.6 [mm]
b_2	6 [mm]
CL	0.27 [mm]
α_{c2}	90 [deg]

The main parameters for the optimised Van der Merwe impeller is shown in Table A.3.

Table A.3: Main Geometrical Parameters for the Van der Merwe optimised Impeller

Parameter	Value
Blade number	7
r_1_hub	8.138 [mm]
r_1_shroud	26.01 [mm]
r_2_shroud	37.5 [mm]
Impeller height	32.976 [mm]
β_{1_hub}	55.017 [deg]
β_{1_shroud}	24.488 [deg]
β_{2}	90 [deg]
LE_hub	2 [mm]
LE_shroud	0.6 [mm]
TE	0.6 [mm]
b_2	6 [mm]
CL	0.27 [mm]
α_{c2}	90 [deg]

The main parameters for the optimised Diener impeller is shown in Table A.4.

Table A.4: Main Geometrical Parameters for the Diener optimised Impeller

Parameter	Value
Blade number	9
r_{1_hub}	10.29 [mm]
r_{1_shroud}	43.43 [mm]
r_{2_shroud}	55.5 [mm]
Impeller height	31 [mm]
β_{1_hub}	49.3 [deg]
β_{1_shroud}	16.7 [deg]
β_{2}	59.1 [deg]
LE _{hub}	2 [mm]
LE _{shroud}	0.6 [mm]
TE	0.002 [mm]
b_{2}	6.94 [mm]
CL	0.02 [mm]
α_{c2}	74.5 [deg]

Appendix B: Mean-Line Code Flow Charts

Three flow diagrams are presented in this appendix. Figure B.1 shows the flow diagram describing the logic of the mean-line code structure. Two of the functions in Figure B.1, "getPerf" and "displayChart", is further expanded in separate flow diagrams in Figure B.2 and Figure B.3 respectively.

The function in Figure B.2 is used to predict the performance, pressure ratio and isentropic efficiency, of an impeller at a specified mass flow rate. This function is therefore used to calculate the design point of the impeller under consideration. The function makes use of three for-loops to calculate the fluid properties at three different locations in the impeller. The first for-loop calculates the fluid properties at the inlet of the impeller, the second for-loop calculates the fluid properties at the throat of the impeller, and the third for-loop calculates the fluid properties at the exit of the impeller. The inlet conditions to each for-loop is taken as the outlet conditions of the previous for-loop. For the first for-loop, user-defined inlet properties are used.

The function in Figure B.3 is used to calculate the performance of the impeller at different operational speeds in order to plot a compressor performance map. The displayChart function basically makes use of the getPerformance function. Incrementation of mass flow is added, together with a number of choke conditions, that enables a curve of pressure ratio or efficiency vs mass flow to be plotted.

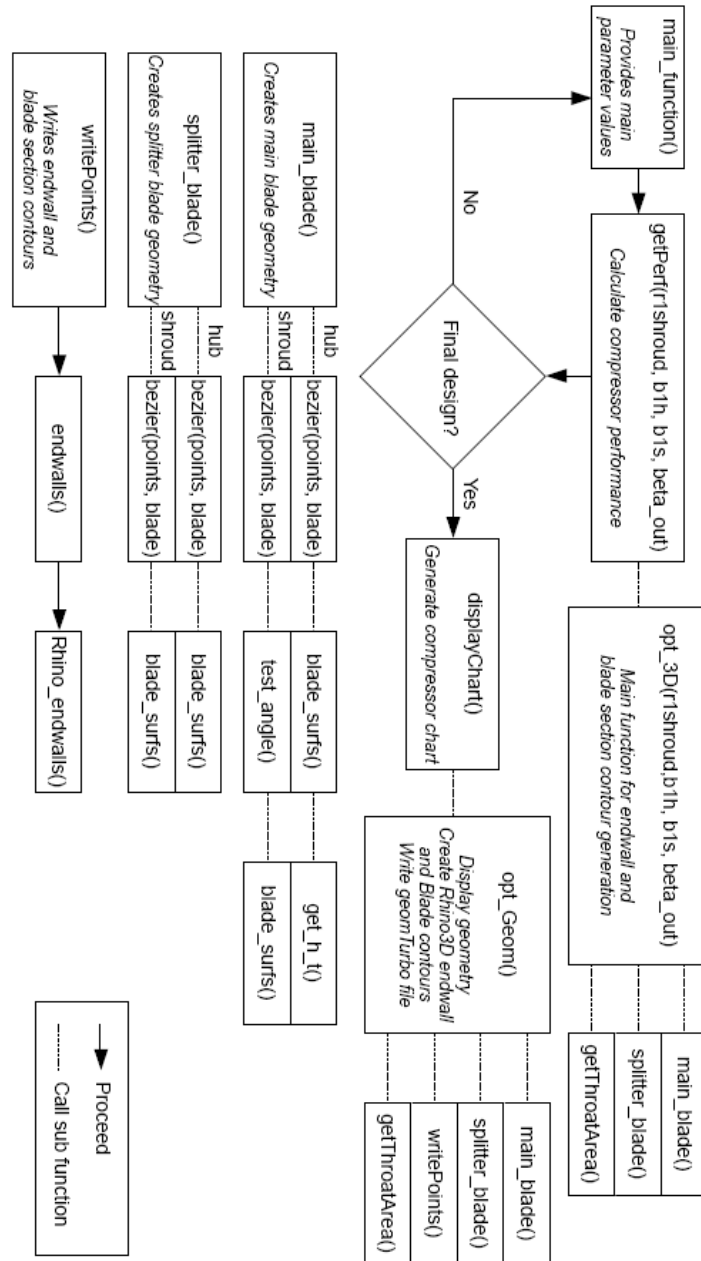


Figure B.1: Flow Diagram of the in-house Design Code (Van der Merwe, 2012)

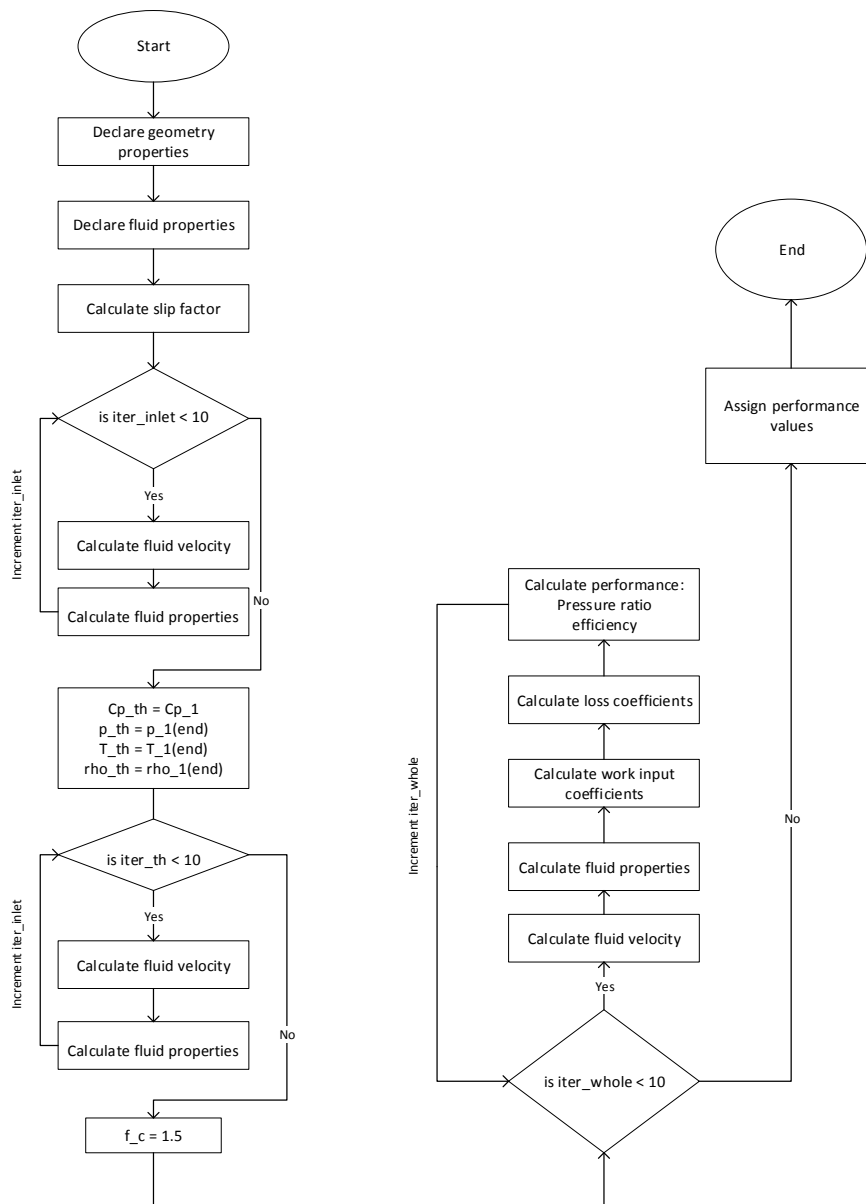


Figure B.2: Flow Diagram for the getPerformance Matlab Script

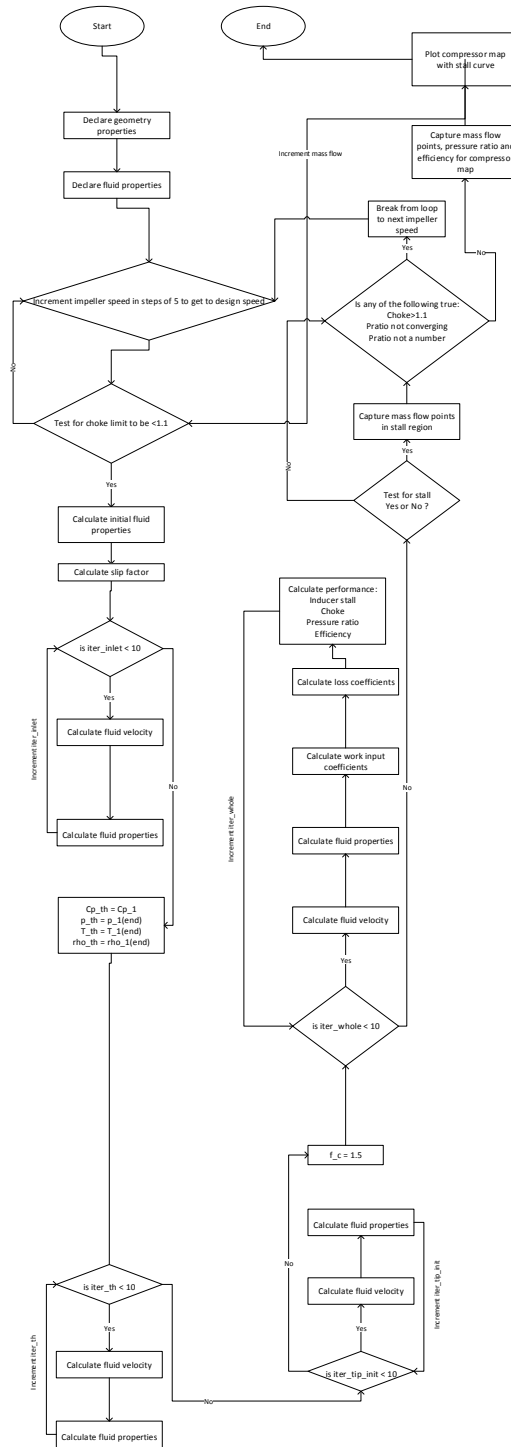


Figure B.3: Flow Diagram for the displayChart Matlab Script

Appendix C: *geomTurbo* File Format

Every *geomTurbo* file starts with a header followed by the hub and shroud endwall curves. The header contains the name of the curve to be defined as well as the coordinate system used and the amount of entries for the specific curve followed by the coordinates defining the curve. The header section for the endwalls is defined as follows:

```
GEOMETRY TURBO
VERSION 5.3
bypass no
NI_BEGIN CHANNEL
units 0.001
NI_BEGIN basic_curve
NAME hub_curve
DISCRETISATION 10
DATA_REDUCTION 0
NI_BEGIN zrcurve
ZR
160
```

The coordinates for the main and splitter blades are also preceded by a header. This header states the number of periodic bounds to be modelled in CFD, suction or pressure side, and the section. The coordinate system and number of coordinate entries once again precedes the coordinates defining the blade. The header for the blades is defined as follows:

```
NI_BEGIN nirow
NAME impeller
TYPE normal
PERIODICITY 7
UNITS 0.001
NI_BEGIN NIBlade
NAME main blade
NI_BEGIN nibladegeometry
TYPE GEOMTURBO
suction
SECTIONAL
2
# section 1
XYZ
496
```

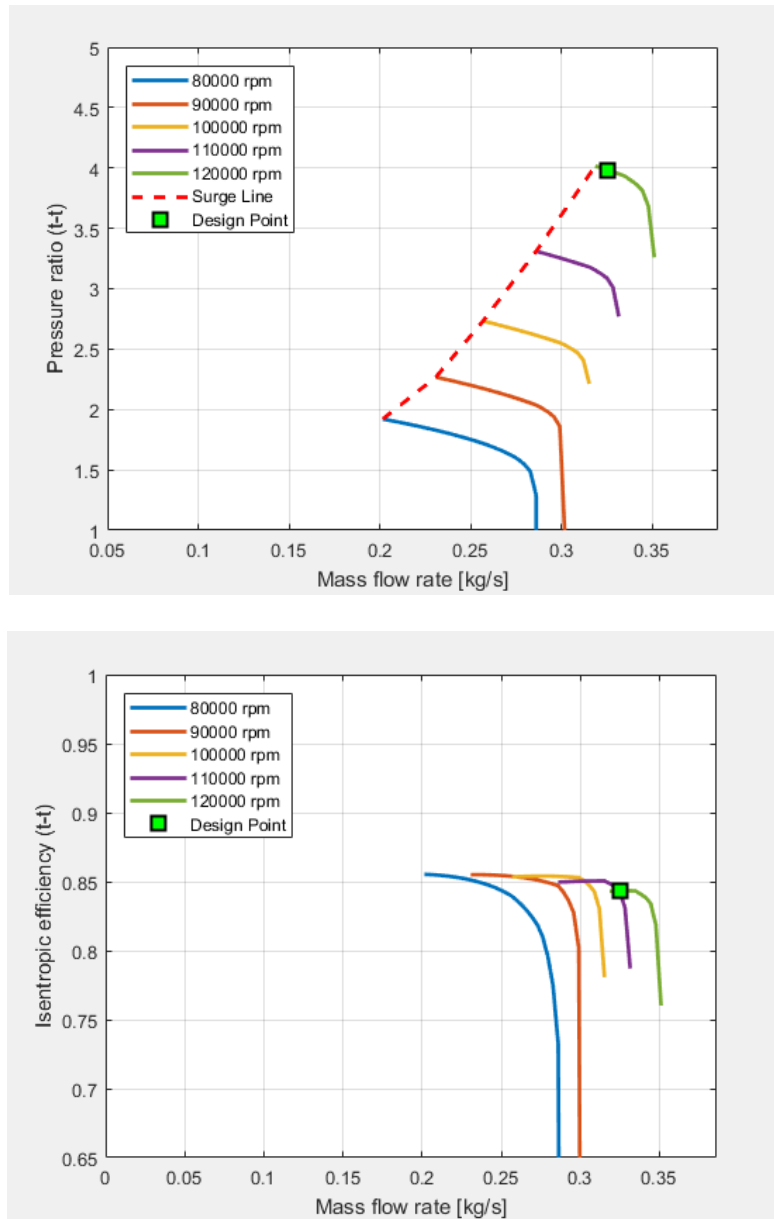
The unit of the coordinate points (millimeters, meters, etc.) is defined by the *units* entry. The number of periodic bounds is given by the *Periodicity* number. As with the hub and shroud endwall curves, the blades are defined starting at the leading edge and moving down towards the trailing edge. The *# section* entry of the file denotes the section number, (1) referring to hub and (2) referring to shroud sections of the blade.

Appendix D: Compressor Maps

The following compressor maps were generated through the in-house mean-line code. The design point is determined by the *getPerf* Matlab[®] script based on the user defined design mass flow rate. Once the design point for the compressor impeller has been determined the *displayChart* script calculates and plot the pressure ratio and efficiency curves for the impeller for five different operating speeds. The operating speeds at which the compressor map is plotted depends on the main operating speed that was defined by the user.

The compressor map for the k27 impeller is shown in Figure D.1. The surge line almost sits on the design point for the 120 krpm curve, with a small operating range predicted. The efficiency for the impeller does not vary that much across the different operating speeds as seen in Figure D.1, all being around 85%.

Figure D.2 shows the compressor map for the mean-line Van der Merwe rotor. Here the design point is closer to the choke region of the predicted operating range for the impeller. Figure D.3 shows the compressor map for the optimised Van der Merwe rotor and Figure D.4 for the optimised Diener rotor. For these rotors the design point sits in the middle of the predicted performance curve. For the optimised Van der Merwe rotor the efficiency decreases substantially for each progressive operation speed. The discrepancy in the efficiency, compared to the other rotors, can be explained by the radial blade outlet angle.

**Figure D.1:** k27 Impeller Compressor Map

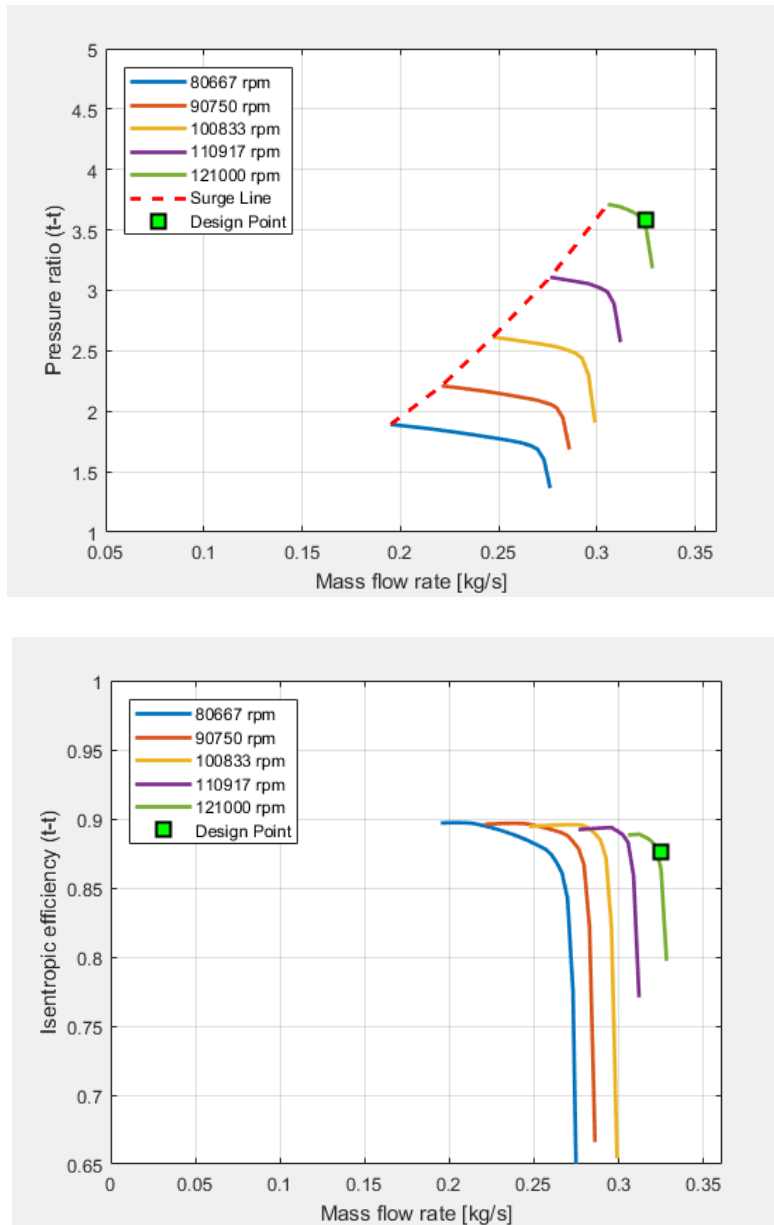


Figure D.2: Van der Merwe mean-line Impeller Compressor Map

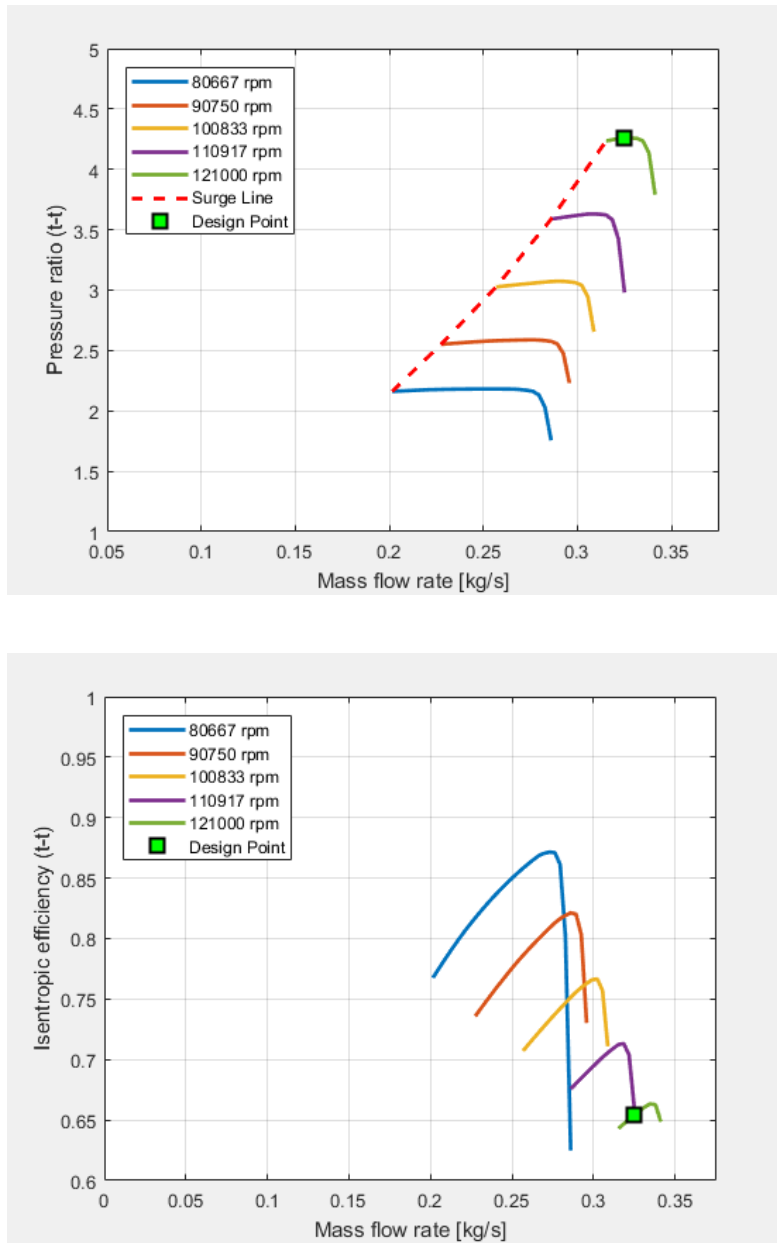
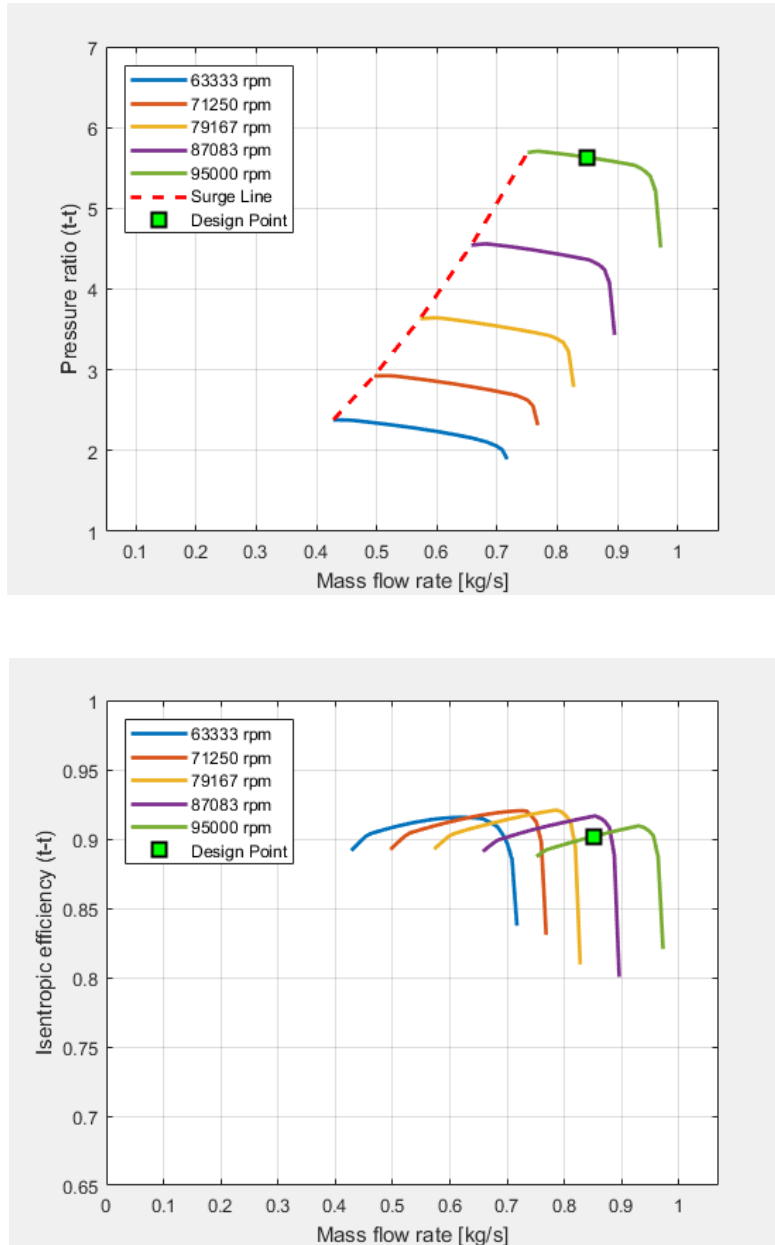


Figure D.3: Van der Merwe Optimised Impeller Compressor Map

**Figure D.4:** Diener Optimised Impeller Compressor Map

Appendix E: CFD Grid Dependency

This appendix contains details for the grid dependency study completed for each of the impellers that were analysed in CFD. A table for each rotor is shown, containing the number of nodes, pressure ratio and efficiency. The number of nodes gives an indication of how coarse or fine the mesh was. The grid dependency was carried out for three different mesh groups, a coarse mesh, medium mesh, and fine mesh. AutoGrid™ allows one of three grid levels to be specified when creating a mesh. The three mesh groups were therefore achieved by creating a mesh on the first grid level (coarse) and selecting the second and third grid levels respectively after saving the previous grid level.

Table E.1 shows the results for the grid dependency study for the k27 impeller. The difference in both pressure ratio and efficiency is within 5% across the three different cell densities.

Table E.1: Mesh Dependency Study for the k27 Impeller

Mesh Property	Coarse	Medium	Fine
Number of nodes	459,540	1,386,316	4,036,308
Pressure ratio	3.704	3.778	3.86
Efficiency	82.027	83.385	84.093

Table E.2 shows the results for the grid dependency study for the optimised Van der Merwe impeller. The difference in both pressure ratio and efficiency is within 5% across the three different cell densities. A higher pressure ratio is recorded for the medium mesh compared to the coarse and fine mesh. This deviation may be caused by a poorer mesh quality compared to the other two meshes.

Table E.2: Mesh Dependency Study for the Van der Merwe Impeller

Mesh Property	Coarse	Medium	Fine
Number of nodes	557,172	1,700,076	4,997,380
Pressure ratio	5.168	5.424	5.166
Efficiency	89.392	91.290	89.262

Table E.3 shows the results for the grid dependency study for the Diener impeller. The largest difference in pressure ratio is 8.66% with the coarse mesh predicting a much lower pressure ratio, while the efficiencies are all within 2% of each other.

Table E.3: Mesh Dependency Study for the Diener Impeller

Mesh Property	Coarse	Medium	Fine
Number of nodes	661,032	2,115,340	6,151,464
Pressure ratio	5.08	5.54	5.51
Efficiency	88.92	87.735	87.471